

University of Nebraska - Lincoln

DigitalCommons@University of Nebraska - Lincoln

Mechanical (and Materials) Engineering --
Dissertations, Theses, and Student Research

Mechanical & Materials Engineering, Department
of

Winter 11-30-2018

Drop Generation Using Cross-Flow in Rigid Body Rotation

Haipeng Zhang

University of Nebraska - Lincoln, haipeng.zhang@huskers.unl.edu

Follow this and additional works at: <http://digitalcommons.unl.edu/mechengdiss>



Part of the [Materials Science and Engineering Commons](#), and the [Mechanical Engineering Commons](#)

Zhang, Haipeng, "Drop Generation Using Cross-Flow in Rigid Body Rotation" (2018). *Mechanical (and Materials) Engineering -- Dissertations, Theses, and Student Research*. 142.

<http://digitalcommons.unl.edu/mechengdiss/142>

This Article is brought to you for free and open access by the Mechanical & Materials Engineering, Department of at DigitalCommons@University of Nebraska - Lincoln. It has been accepted for inclusion in Mechanical (and Materials) Engineering -- Dissertations, Theses, and Student Research by an authorized administrator of DigitalCommons@University of Nebraska - Lincoln.

Drop Generation Using Cross-Flow in Rigid Body Rotation

By

Haipeng Zhang

A THESIS

Presented to the Faculty of

The Graduate College at the University of Nebraska

In Partial Fulfillment of Requirements

For the Degree of Master of Science

Major: Mechanical Engineering and Applied Mechanics

Under the supervision of Professor Sangjin Ryu

Lincoln, Nebraska

November, 2018

Drop Generation Using Cross-Flow
in Rigid Body Rotation

Haipeng Zhang, M. S.

University of Nebraska, 2018

Advisor: Sangjin Ryu

Inspired by crossflow membrane droplet generation and microfluidic droplet generation, I propose an easy method to generate monodisperse drops using cross-flow caused by rigid body rotation. In this approach, a dispersed phase (DP) liquid was injected through a stationary vertical needle into an immiscible continuous phase (CP) liquid which was in rigid body rotation. A DP drop growing at the end of the needle experienced fluid dynamic forces from the horizontal CP flow, and it was detached from the needle when it had grown to a certain size. This study investigated the relationship between the resultant size of drops and the controllable experimental factors including the flow velocity of the CP at the needle end and the flow rate of the DP through the needle.

ACKNOWLEDGEMENTS

Firstly, I would like to thank the harsh life. The difficulty of life pushed me forward.

I would like to thank my advisor, Dr. Sangjin Ryu, for the help of my research and the advice of daily life. I would like to thank Dr. Jae Sung Park and Dr. Seunghee Kim for helping me through my research career and being my thesis committee.

I would like to thank Dr. Howard Stone in Princeton University for discussion. I would like to thank Dr. Timothy Wei for the macro lens of high-speed camera. I also would like to thank Ali Mazaltarim in the Department of Chemistry for the help of surface tension coefficient measurement.

I would like to thank my lab mates, Donghee Lee, Jacob Gottberg, Tomer Palmon, Dilziba Qizghin, and Stephanie Vavra, for their help of my research and support in the laboratory. I would like to thank the lab members in Park Research Group, Ethan Davis, Siamak Mirfendereski, and Thomas Hafner, for the discussions of my research. I also would like to thank Luz Sotelo for helping me to improve my presentation.

I would like to thank Terri Eastin in the office of graduate studies, Kathie Hiatt, Mary Ramsier, Cherie Crist, Heidi Krier, and other staffs in the department office, for helping me to get the master's degree. I would like to thank Alan Wilkins in ISSO for the supporting information of graduate studies. I also would like to thank the Lincoln Literacy, Clay Farris Naff, Rik Minnick, and other staffs' help about the language and our lives in the United States.

I would like to thank the faculties of the Kitami Institute of Technology in Japan,

Hiroshi Sakamoto, Hiroyuki Haniu, and Kazunori Takai, for leading me into the scientific research career.

I would also like to thank the members of the pump department of Kubota Corporation in Japan, Hirohiko Yamada, Teruo Miura, Makoto Sano, Hiroyuki Ishimi, and Kazuo Nishimura. I couldn't become a graduate student without their support.

Finally, I would like to thank my family. My parents Jianfeng Zhang and Zhiquan Duan, my parents-in-law Litan He and Dongmei He are supporting me continuously. I would like to thank my wife, Ling He. She is always staying with me to against hard time.

Table of Contents

ACKNOWLEDGMENTS.....	iii
List of Figures.....	vii
List of Tables.....	x
Chapter 1 Introduction.....	1
1.1 Crossflow-based Drop Generation Methods.....	2
1.1.1 Membrane Emulsification Method.....	3
1.1.2 Crossflow-based Microfluidic Drop Generators.....	4
1.2 Pinch-off Principles of Drop Generation Process in Crossflow.....	6
1.2.1 The Squeezing Mode in Crossflow.....	7
1.2.2 The Dripping Mode in Crossflow.....	9
1.2.3 The Jetting Mode in Crossflow.....	10
1.3 The Models for Drop Sizes Prediction in Crossflow.....	11
1.3.1 The Dimensionless Parameter-based Map.....	12
1.3.2 The Nondimensional Number-based Map.....	13
1.3.3 The Torque Balance Equation.....	17
1.4 Rigid Body Motion Driven Crossflow-based Drop Generation.....	18
1.4.1 Motivation.....	18
1.4.2 Working Principle.....	19
Chapter 2 Methods and Materials.....	22
2.1 Materials.....	22
2.2 Experimental Setup.....	26

2.3 Experimental Procedures.....	30
2.4 Image Correction.....	32
2.5 Image Processing of Drops.....	36
Chapter 3 Results.....	39
3.1 Experimental Images and Drop Pinch-off Modes of the Drops.....	39
3.2 Drop Diameter Distribution.....	48
3.3 Dimensionless Phase Diagram of the Drop Generation.....	52
3.4 The Different Pinch-off Zones in the Nondimensional Analysis Phase Diagram.....	54
3.5 The Application of the Nondimensional Analysis Phase Diagram.....	56
Chapter 4 Discussion.....	58
4.1 Absence of the Squeezing Mode.....	58
4.2 Controlling Drop Diameter.....	58
4.3 Nondimensional Numbers in the Drop Generation Processes.....	60
4.4 The Studies of Force Balanced Equation.....	66
Chapter 5 Conclusions.....	71
Appendix A. The Measurement Results of Drop Sizes.....	73
Appendix B. The Size Distributions of Generated Drops.....	77
Appendix C. The Calculation of Dimensionless Parameters.....	94
Appendix D. The Calculation of Nondimensional Numbers.....	98
Appendix E. The Calculation of Torque Balance Equation.....	106
References.....	110

List of Figures

Figure 1-1. The working process of drop-based cell encapsulation method.	1
Figure 1-2. The schematic figure of the principle of the crossflow-based drop generation.....	3
Figure 1-3. The schematic figure of the membrane emulsification method.....	4
Figure 1-4. The schematic figure of the T-junction microfluidic drop generator.....	5
Figure 1-5. The schematic figure of other microfluidic drop generators.....	6
Figure 1-6. The images of the squeezing mode, the dripping mode, and the jetting mode-based drop generation in the T-junction device.....	7
Figure 1-7. The formation process of the drops in the squeezing mode.....	8
Figure 1-8. The formation process of the drops in the dripping mode.....	10
Figure 1-9. The formation process of the drops in the jetting mode.....	11
Figure 1-10. An example of the dimensionless parameter-based map for drop generation.....	13
Figure 1-11. An example of the nondimensional number-based map for drop generation.....	15
Figure 1-12. An example of $Ca-We-Oh$ -based map for pinch-off modes.....	16
Figure 1-13. The experimental setup for the $Ca-We-Oh$ -based map example.....	16
Figure 1-14. An example of $We-Ca/Oh$ -based map for pinch-off modes.....	17
Figure 1-15. The experimental setup for the $We-Ca/Oh$ -based map example.....	17
Figure 1-16. The schematic of TBE model in drop generation.....	18
Figure 1-17. The principle of the rigid body motion driven drops generation system...	20

Figure 1-18. The schematic figure of the rigid body motion driven drops generation system.....	20
Figure 2-1. The viscosity measurement results of the rheometer.....	24
Figure 2-2. The interfacial surface tension coefficient measurement results of the goniometer.....	25
Figure 2-3. Experiment setup of drop generation.....	26
Figure 2-4. The grid plate attached on the needle holder for image correction.....	31
Figure 2-5. A reference image of the grid plate in the continuous phase.....	31
Figure 2-6. A raw image of drop generation processes ($R = 80$ mm, $\Omega = 4.7$ rad/s, and $Q_d = 0.5$ mL/min.).....	33
Figure 2-7. The x and y coordinates measurements of the intersection points from the reference image.....	34
Figure 2-8. A cropped raw image of drop generation processes.....	35
Figure 2-9. An adjusted image of drop generation processes.....	35
Figure 2-10. The measurement processes of drops in the ADM.....	37
Figure 3-1. The drop generation process of $V_c = 210.42$ mm/s, and $V_d = 543.67$ mm/s..	40
Figure 3-2. The drop generation process of $V_c = 210.42$ mm/s, and $V_d = 2174.68$ mm/s.....	40
Figure 3-3. Drop size distribtion of $V_c = 140.3$ mm/s or 189.0 mm/s, $V_d = 543.7$ mm/s, $D_{needle} = 0.14$ mm.....	49
Figure 3-4. The histograms of $V_c = 140.28$ mm/s or 189.04 mm/s, $V_d = 2174.68$ mm/s, $D_{needle} = 0.14$ mm.....	50

Figure 3-5. The map of the nondimensional analysis phase diagram.....	53
Figure 3-6. The zones of pinch-off modes in the nondimensional analysis phase diagram.....	55
Figure 3-7. The applications of the nondimensional analysis phase diagram.....	57
Figure 4-1. The nondimensional number-based map ($Ca-We$).....	61
Figure 4-2. The prediction of the pinch-off zones in $Ca-We$ map.....	62
Figure 4-3. The nondimensional number-based map ($Ca/Oh_{CP}-We$).....	64
Figure 4-4. The comparison of nondimensional number-based map ($Ca/Oh-We$).....	65
Figure 4-5. The schematic figure of TBE in this study.....	67
Figure 4-6. The comparison of D_{drop} between TBE and experimental data. ($D_{needle} = 0.14$ mm).....	69
Figure 4-7. The comparison of D_{drop} between TBE and experimental data. ($D_{needle} = 0.32$ mm).....	70

List of Tables

Table 2-1 The measurement results of mass (unit: g).....	23
Table 2-2. The measured properties of the CP and the DP.....	25
Table 2-3. The experimental conditions applied for the drop generation processes....	28
Table 2-4. V_c values calculated from the experimental conditions.....	29
Table 2-5. V_d values calculated from the experimental conditions.....	29
Table 2-6. The calculation results of tilted angles and elongated aspect ratios.....	35
Table 2-7. Pixel size for different experimental conditions.....	36
Table 3-1. Drop generations with $D_{needle} = 0.14$ mm (scale bar = 1 mm).....	41
Table 3-2. Drop generations with $D_{needle} = 0.32$ mm (scale bar = 1 mm).....	44
Table 3-3. The comparison of drop monodispersity between different methods.....	51
Table A-1. The drop diameters with various experimental conditions.....	73
Table B-1. The histograms of experiments with $D_{needle} = 0.14$ mm.....	77
Table B-2. The histograms of experiments with $D_{needle} = 0.32$ mm.....	83
Table B-3. The calculation results of CV.....	90
Table C-1. The parameters of the nondimensional analysis.....	94
Table D-1. The calculations of the nondimensional numbers (Ca and We).....	98
Table D-2. The calculations of the nondimensional numbers (Oh_{CP} and Ca/Oh_{CP})...	102
Table E-1. The calculations of D_{drop} using TBE.....	106

Chapter 1 Introduction

A drop is a deformable liquid sphere with limited volume and high surface-area-to-volume ratio. Drops are widely used in multiple areas for various purposes, including industrial applications and scientific researches [1, 2]. Drops can be used for changing the physical properties of emulsions. For example, the viscosity of emulsion can be changed by varying shear rates on drops because of their deformability. A similar application was developed for changing the elasticity of emulsion based on the surface tension difference of drops [3, 4]. Additionally, drops are used to control chemical or biochemical reactions as microreactors. There are several advantages of the drop-based microreactor: less reagent consumption because of the limited volume of drops, and faster reaction processes because of the high surface-area-to-volume ratio [5]. Furthermore, drops are used in complicated experimental systems for cells minor control. Figure 1-1 is an example of the drop-based cell encapsulation method in a drop generation system. The drops containing cells are delivered to the downstream direction for further manipulations [6].

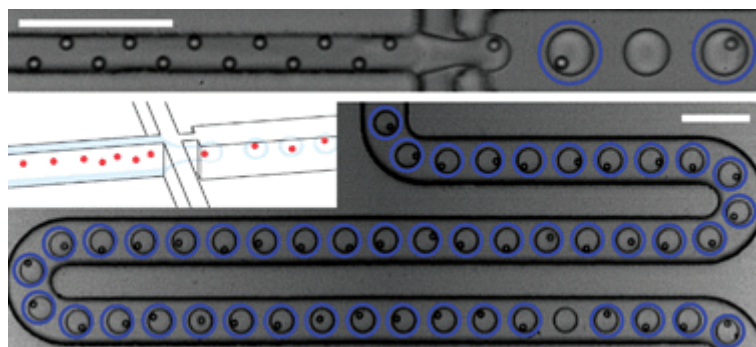


Figure 1-1 The working process of drop-based cell encapsulation method [7, 8].

(Scale bar: 100 μm)

Because of the various applications of drops in chemistry, electronics, cosmetics, foods, and pharmaceuticals, the requirements of monodispersed drop generators have been increasing [9-11]. A well-designed drop generator must be able to generate drops continuously with predictable sizes. The focus of this study is to develop a reliable drop generator for easier and cheaper production of monodispersed drops in the laboratory.

1.1 Crossflow-based Drop Generation Methods

Many different drop generation methods were developed in the past years. A well-known subgroup is the crossflow-based drop generation methods [12-18]. Figure 1-2 shows the principle of the crossflow-based drop generation. Two immiscible liquid phases, the continuous phase (CP) and the dispersed phase (DP), are injected into a device with a certain designed channel structure [19]. The structure can lead the stream of the CP and DP meet with each other. The interface between these two phases occurs where the CP and DP meet [2, 20]. The interface deforms while the CP and DP are injected. Eventually, a certain amount of the DP is pinched-off from the stream of DP. The separated portion of the DP becomes spherical shape automatically because of the surface tension. Afterwards, the drops are delivered by the CP in the direction of the CP flow. By injecting the CP and DP continuously, the drop generation process can be continued [4]. Based on the basic principle of the crossflow, different crossflow-based drop generators have been developed.

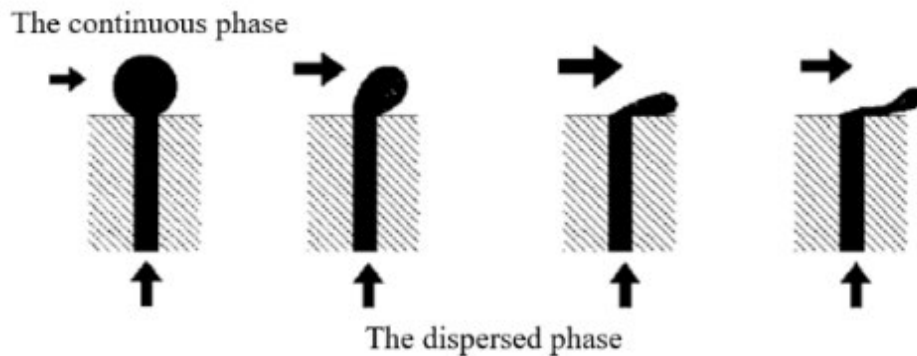


Figure 1-2 Schematic figure of the principle of the crossflow-based drop generation

[13].

1.1.1 Membrane Emulsification Method

The membrane emulsification method is developed based on the crossflow [13, 15]. Because of the high frequency of drop generations, the method has drawn attentions and is widely used in industrial areas. Figure 1-3 is a schematic figure of the membrane emulsification method. The DP is injected through multiple pores or capillary tubes of a flat membrane at a volume flow rate Q_d . The CP is flowed with volume flow rate Q_c in the direction parallel to the membrane surface. Depending on the Q_d , a part of the DP stream passing through the pores become spherical at the surface of the membrane. After the spherical DPs grow to certain sizes, the shear force caused by CP acting along the membrane surface can separate the spherical DPs from the DP streams. Due to the high numbers of the pores in the membrane, huge amount drops are pinched-off when the CP swept the surface of the membrane.

For different requirements, minor changes such as the shape of the membrane are

considered for the membrane emulsification method [2]. The shape of the membrane does not have to be flat. Cylindrical tube-shaped membranes are also used for easier collection of drops. Different geometry designs of the membrane structures and the experimental conditions of the working fluids are used for various purposed applications [13, 15, 21-31].

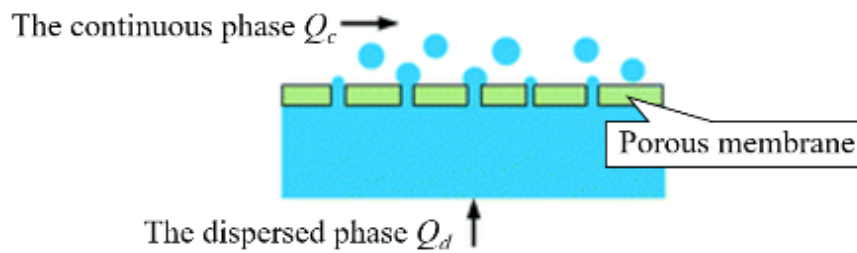


Figure 1-3. The schematic figure of the membrane emulsification method [2].

1.1.2 Crossflow-based Microfluidic Drop Generators

The crossflow-based microfluidic drop generators are another series of drop generation method. The CP and DP are injected through tubing into a microfluidic device with micro-scales channels inside. The micro channels define the flow directions of CP and DP, the positions where CP meet with DP, and an angle θ ($0^\circ < \theta \leq 180^\circ$) between the flow directions of the two immiscible phases. The selection of the materials for making microfluidic devices is flexible. The polydimethylsiloxane (PDMS), glass, and 3D printed materials are used [2, 32]. Because of the micro-scaled device, the crossflow-based microfluidic drop generators are well used in laboratory for drop generation with sensitive controlling.

Figure 1-4 is a well-known design of the microfluidic PDMS drop generation devices named as the T-junction device [33, 34]. The T-junction device is a simple design which is good for microfluidic research. 3 holes on the device are used as the inlet of the CP, the inlet of the DP, and the outlet of the drops, respectively. The volume flow rate of CP and DP are applied as Q_c and Q_d , respectively. The width of the channels for the inlet of the continuous phase, the inlet of the dispersed phase, and the outlet are indicated as w_c , w_d , and w_o , respectively. The flow directions of the CP and DP are following the direction of the micro channels. At the junction, CP meet with DP at 90° , and then break a drop from the stream of DP. By using the T-junction microfluidic device, the drops of DP are generated continuously to the outlet.

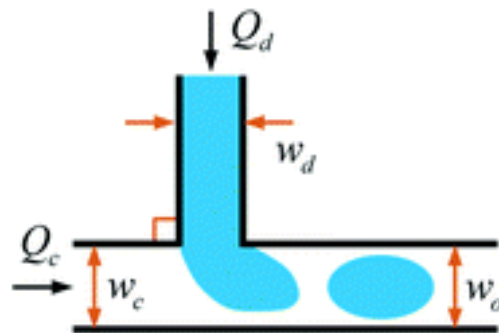


Figure 1-4. The schematic figure of the T-junction microfluidic drop generator [2].

The similar idea but different micro channel designs are also used. Figure 1-5 a-d are other crossflow-based microfluidic device designs. Figure 1-5a is the T-junction with θ other than 90° ($0^\circ < \theta \leq 180^\circ$). Figure 1-5b is named as Head-on geometry device with $\theta = 180^\circ$. Figure 1-5c is the Y-shaped junction. Figure 1-5d is the double T-junction because of the combined shape of two T-junctions [35]. For specific requirements or working conditions, some accessories, such as a piezo electric bending disc, can be used in the microfluidic system for promoting the formation processes of drops [11].

Different novelties are included in these designs, but the basic ideas of drop generation processes are the same as in the T-junction device.

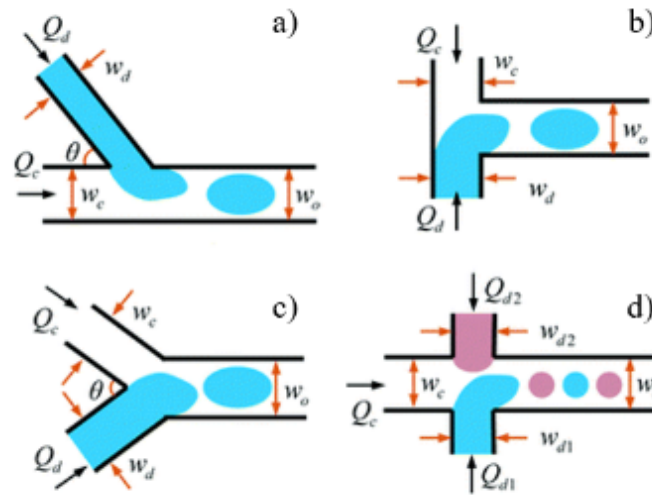


Figure 1-5. The schematic figure of other microfluidic drop generators [2].

1.2 Pinch-off Principles of Drop Generation Process in Crossflow

In order to satisfy the requirements of different purposes, the sizes of drops generated from the devices should be predictable. Since the experimental data revealed that the range of drop sizes are various for different pinch-off modes, the studies of drop size predictions are started from understanding the principles of drop pinch-off modes [2, 21].

Three pinch-off modes, the squeezing mode, the dripping mode, and the jetting mode, are identified in the various crossflow-based drop generators [2, 21, 36]. For demonstration, the pinch-off processes of drops in the T-junction microfluidic PDMS device are studied. Figure 1-6 a-c shows the images of these three pinch-off modes in the T-junction device. Each pinch-off mode has the corresponding experimental

conditions of Q_c and Q_d . The T-junction device is a simple design for understanding the pinch-off processes, so it is used for the following explanations of the pinch-off modes in crossflow.

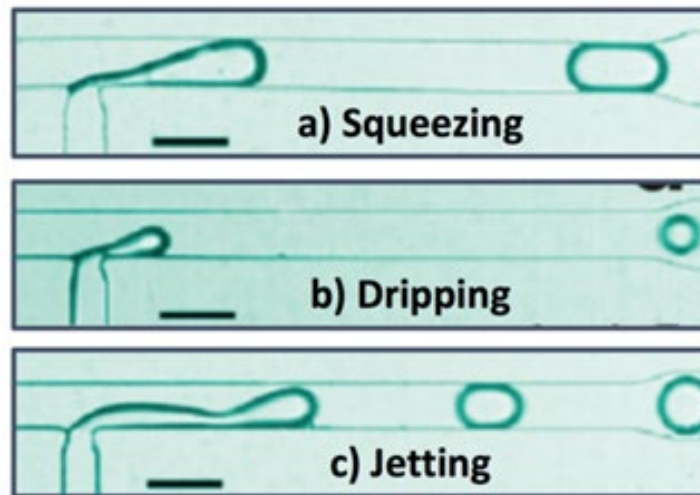


Figure 1-6. The images of the squeezing mode, the dripping mode, and the jetting mode-based drop generation in the T-junction device [2].

1.2.1 The Squeezing Mode in Crossflow

The squeezing mode is observed in the crossflow-based generation method but only in a fluidic channel with surrounded geometries, such as T-junction or Y-junction devices. When the injected DP is confined in a microfluidic channel, the squeezing mode occurs. Figure 1-7 is using the T-junction device as an example to show the drop formation process of the squeezing mode.

The geometry of the device is important for the drop generation in the squeezing mode. A liquid phase of the DP is injected into the T-junction microfluidic device. Because of the pressure of injection, the liquid phase of DP in the channel can reach the

wall of the channel and grow continuously in the channel toward the outlet after passing the junction. Eventually, the channel is clogged by the liquid phase of DP. The flow direction of CP is the same as the liquid phase, so CP is stopped in the channel. A huge pressure difference between the both sides of the DP phase occurs because of the growing DP phase and the injection of CP. Once the pressure difference between the both sides of DP clog is high enough, the connection of the injected DP and the DP clog in the channel will be broken. The elongated-shaped clog of the DP is pushed away by the CP flow toward the outlet of the channel. After leaving the surrounded boundaries of the channel, the clog of DP can become spherical automatically because of the surface tension [36].

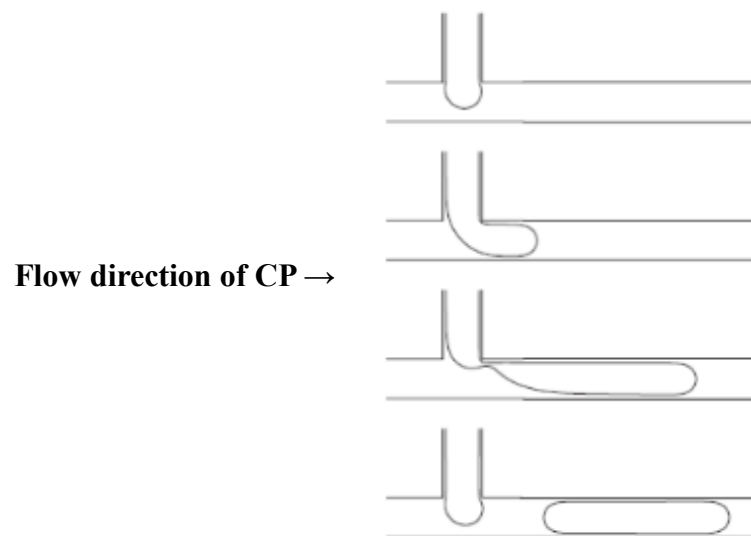


Figure 1-7. The formation process of the drops in the squeezing mode [37].

Two characteristics of the drops in the squeezing mode can be found. The first one is the larger sizes of the drops. The total volume of the drops in the squeezing mode can be approximately calculated as the product of the cross-section area of the channel and the length of the clog. The second one is the requirement of the surrounded geometry.

Without a channel confining the DP, the pressure difference between the both sides of the DP cannot support the squeezing mode. For instance, there is no drop in the squeezing mode observed in the membrane emulsification method. Because the DP in the membrane emulsification method is not confined after passing through the pores, the pressure difference among a spherical-shaped DP on the surface of the membrane is negligible. Without the high enough pressure difference, the squeezing mode does not occur [36, 37].

1.2.2 The Dripping Mode in Crossflow

The formation process of the dripping mode is shown in Figure 1-8. The detachment of the dripping mode occurs at the junction. The liquid phase of DP can pass over the subchannel when the DP is injected. In the meantime, the CP is injected from the left side of the channel. The flow direction of the CP is the same as the main channel, so CP is sweeping through the junction where the DP is growing. The shear force from the flow of CP is acting on the growing DP with other forces such as the buoyance force and the surface tension force. For a certain volume of the spherical DP, these forces arrived as equilibrium state. Thus, the drop of DP breaks from the junction as a critical size of D_{drop} [37].

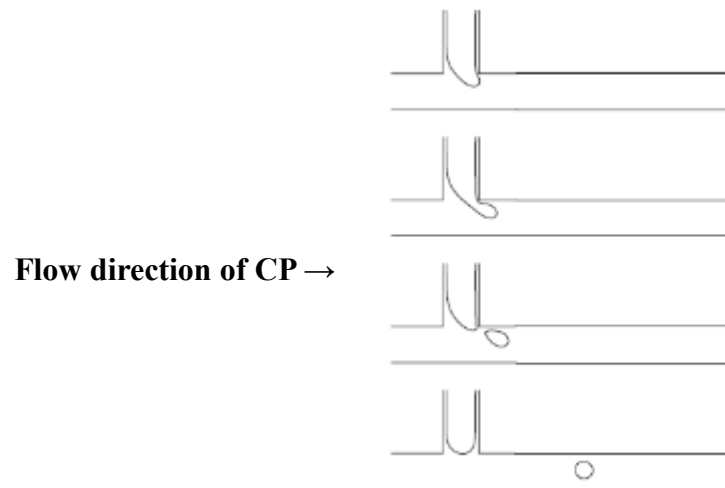


Figure 1-8. The formation process of the drops in the dripping mode [37].

1.2.3 The Jetting Mode in Crossflow

The jetting mode is observed at the tip of an elongated DP stream from the junction in the microfluidic channel. The DP should be injected with high Q_d to prevent the pinch-off at the junction. A stream of the DP flows with the same direction as CP in the main channel as Figure 1-9 shows. The drops are generated from the tip of the DP stream far away from the junction. To distinguish the jetting mode and the dripping mode, a well-used definition of jetting mode is that the length of the jetting DP stream elongated from the junction (L in Figure 1-9) should be longer than D_{drop} ($L > D_{drop}$) [38]. The reason of drop generation in the jetting mode is the instability of the stream. Elongated stream increased the surface area of the DP phase significantly. The tendency of minimizing the surface area of drops triggered the instable wave shaped stream. Eventually, the tip of steam is raptured as multiple drops, and the drops are smaller than the drops in the dripping mode [21].

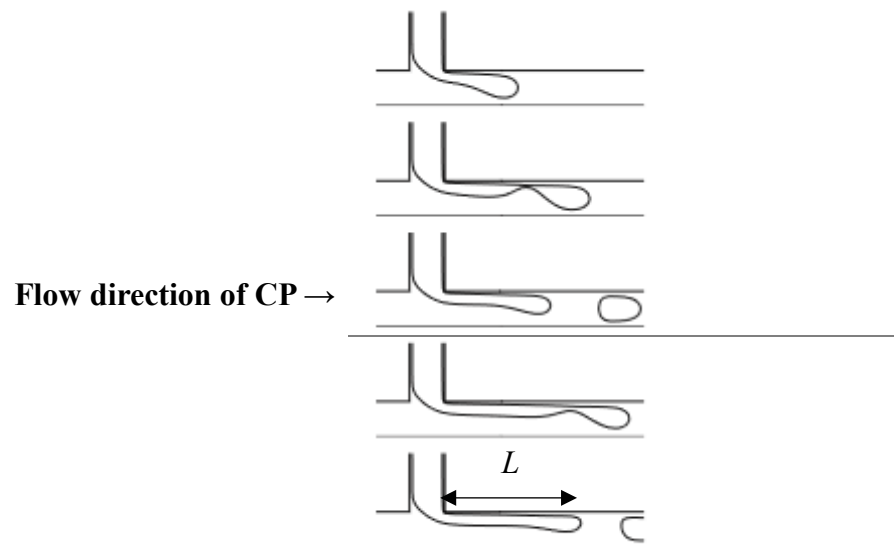


Figure 1-9. The formation process of the drops in the jetting mode [37].

Modifying experimental conditions can change the patterns of drop generations, even though using the same drop generation devices. In general, when the Q_d is increased, the pinch-off mode can be switched from the dripping mode to the jetting mode.

1.3 The Models for Drop Sizes Prediction in Crossflow

According to the applications, the requirement of D_{drop} can be different. It is important to predict the size of products in the generation processes. From the studies of the pinch-off modes in drop generation process, several models have been developed. Three models from the view of applications and physical principles are introduced in the section.

1.3.1 The Dimensionless Parameter-based Map

In the drop generation process, several controllable variables can be changed for a chosen fluidic drop generator. Since the number of variables is already determined by the design of the drop generator, it will be benefits to have reference values for D_{drop} prediction. A simple way is to calculate the dimensionless parameters from the experimental data of D_{drop} and controllable variables. The summarized plot of the relationship between D_{drop} and controllable variables can be used for checking the experimental conditions to generate desired sized drops [36].

Figure 1-10 is an example of maps based on the dimensionless parameters. The used device is a T-junction device with given geometries making drops in the squeezing mode. Oil and water are used as the CP and DP, respectively. The controllable variables of the drop generation system are the volume flow rate of the CP and DP (Q_{oil} and Q_{water}). Because of the shape of drops in the squeezing mode, two parameters, the length and the width of the DP clog (L and w), are used to evaluate the size of the generated drops.

Figure 1-10 summarized experimental data of the size of drops and the applied Q_{oil} and Q_{water} . The desired D_{drop} can be found in the map, and the corresponding Q_{oil} and Q_{water} is the solution of the experimental conditions. The map is easy to use for predicting D_{drop} , but the data collection is necessary for every new design of drop generator. Also, if the process of drop generation has been changed, such as the working fluids have been replaced with different materials, the map is invalid. Experimental data

collection and the map plotting must be repeated.

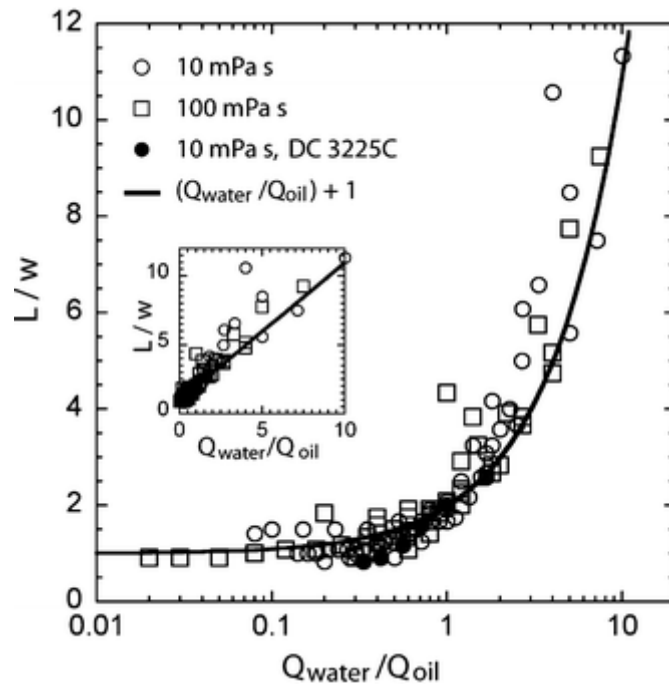


Figure 1-10. An example of the dimensionless parameter-based map for drop generation [36].

1.3.2 The Nondimensional Number-based Map

Nondimensional numbers are also used to predict the processes of drop generations. From the previous discussion, the ranges of D_{drop} in each pinch-off mode are different. In the jetting mode, D_{drop} is smaller than in the dripping mode. So the prediction of the pinch-off mode can also related with D_{drop} .

The dripping-to-jetting behavior of drop generation can be predicted by Capillary number (Ca) and Weber number (We) [39-41]. Ca is considered as the ratio of viscous drag force and the surface tension force, and We is the ratio of inertia force and the surface tension force in the drop generation process. For example, smaller Ca means

that the viscos drag force acting on the drop generation process is smaller than the surface tension force. The importance of the viscos drag force, the surface tension force, and the inertia force acting on the system can be evaluated by these numbers.

Ca and We are calculated as Eq. (1-1) and Eq. (1-2) [42]. μ_c and μ_d are the dynamic viscosity of the CP and the DP, respectively. V_c and V_d are the linear flow speed of the CP and the DP, respectively. ρ_d is the density of the DP. D_{needle} is the inner diameter of the needle, which indicates the characteristic length in this equation. And, σ is the interfacial tension between the CP and DP.

$$Ca = \frac{\mu_c V_c}{\sigma}, \quad (1-1)$$

$$We = \frac{\rho_d V_d^2 D_{needle}}{\sigma}, \quad (1-2)$$

For smaller Ca of the DP, drops are generated in the jetting mode because the effect of shear stress acting on the stream of DP is relatively small. The drops cannot be separated by CP from the position where DP meet with CP immediately. In a T-junction device, the DP can grow continuously till the DP clogging the main channel. Based on the explanation of the squeezing mode, DP drop only pinch-off when the pressure difference acting on the both sides of the clog is high enough. However, the jetting mode of drop generation can be related with bigger Ca [36]. Figure 1-11 is an example of Ca and We from a membrane emulsification method. Each symbol in the map indicates different working fluids as DP, and the hollow markers and the solid markers mean the dripping mode and the jetting mode, respectively [21]. From the map, the jetting mode always occur with high value of Ca and We .

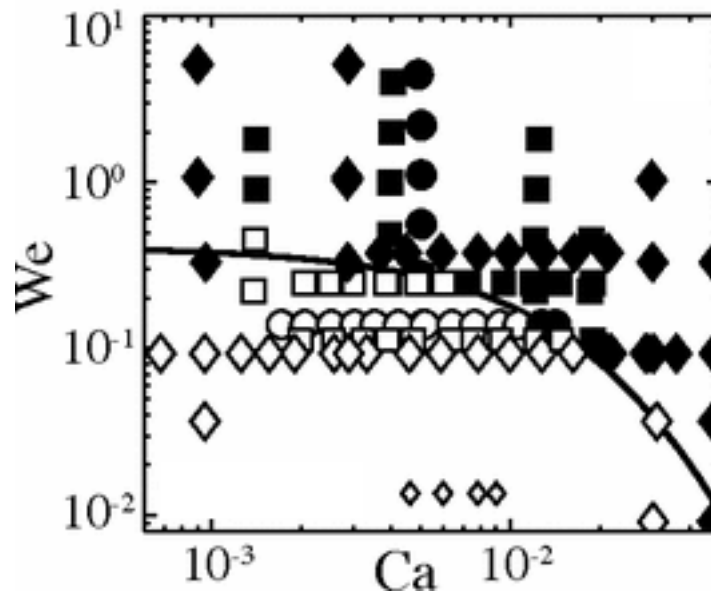


Figure 1-11. An example of the nondimensional number-based map for drop generation [21].

Another nondimensional number, Ohnesorge number (Oh), are used to evaluate the difference of the dripping to jetting transition (DJT) in various fluids [21, 38]. Oh is the ratio of viscous force and the square root of inertia force times surface tension force. The Oh of CP can be calculated as Eq. (1-3).

$$Oh_{CP} = \frac{\mu_c}{\sqrt{\rho_c D_{needle} \gamma}} \quad (1-3)$$

Figure 1-12 shows the DJT of drop generation as Ca - We - Oh map. Oh of DP was used in this map. The Ca - We -based map will be different for different Oh_{DP} [21, 38]. Different liquids were used for collecting data on the map, and the experimental setup of this study is shown as Figure 1-13.

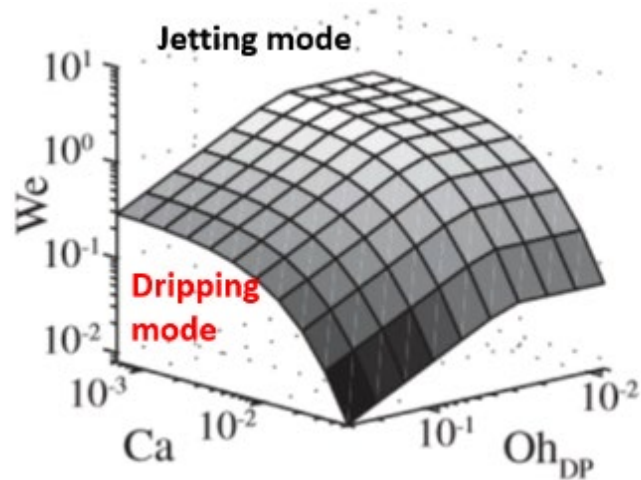


Figure 1-12. An example of Ca - We - Oh -based map for pinch-off modes [21].

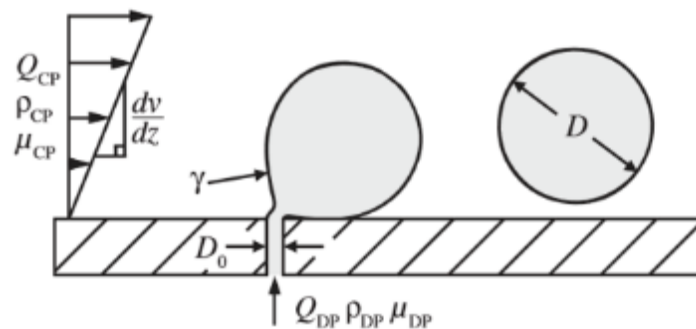


Figure 1-13. The experimental setup for the Ca - We - Oh -based map example [21].

Another example of nondimensional number-based map is Figure 1-14. Oh_{CP} is combined with Ca of CP (Ca_{out} in the map) as x-axis. We of DP (We_{in} in the map) is the y-axis. The experimental setup of this study is shown as Figure 1-15, which is similar with the previous example.

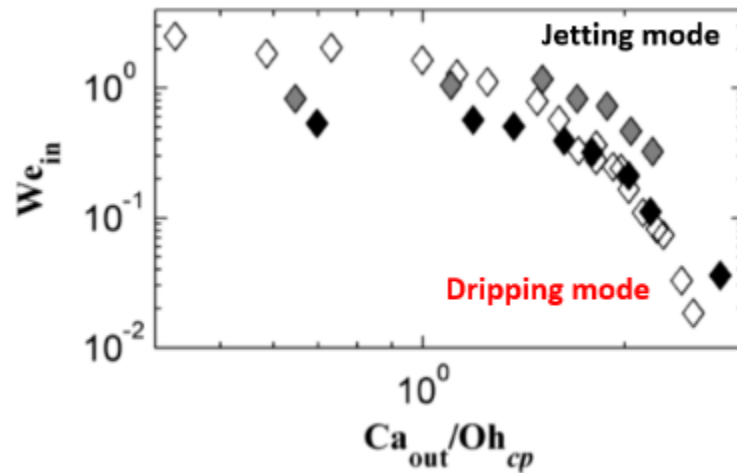


Figure 1-14. An example of Ca/Oh - We -based map for pinch-off modes [38].

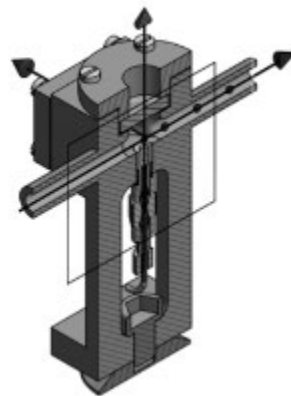


Figure 1-15. The experimental setup for the Ca/Oh - We -based map example [38].

1.3.3 The Torque Balance Equation

Torque balance equation-based analysis (TBE) is another theoretical model for the prediction of D_{drop} [13, 27-29, 31, 43-45]. Figure 1-16 is a schematic figure of the TBE model for membrane emulsification. The drop diameter is D_d at the surface of the membrane. The DP is injected upwards and growing from the pore (diameter = D_p) as height h , and the flow direction of CP is from left to right. Buoyance force (F_{BG}), dynamic lift force (F_{DL}), Young-Laplace force (F_{YL}), drag force (F_{DR}), and interfacial

tension force (F_γ) are acting on the drop [12, 25, 29, 43, 46-51].

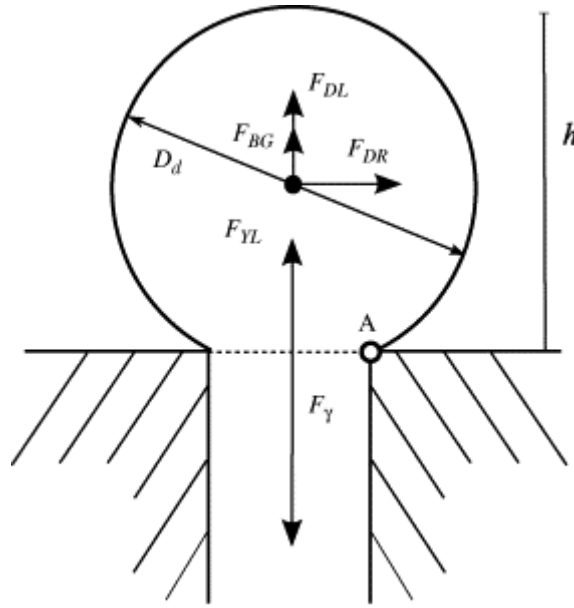


Figure 1-16. The schematic of TBE model in drop generation [43].

If the drop is considered as a rigid spherical object in the TBE model, point A is the pivot point for the equilibrium of torque. Choosing $\frac{D_p}{2}$ and $h - \frac{D_d}{2}$ as moment arms, the TBE can be written as Eq. (1-4) to solve D_{drop} [43].

$$F_{DR} \left[h - \frac{D_d}{2} \right] = (F_Y - F_{YL} - F_{DL} - F_{BG}) \frac{D_p}{2}, \quad (1-4)$$

1.4 Rigid Body Motion Driven Crossflow-based Drop Generation

1.4.1 Motivation

Different drop generators in crossflow are introduced in the previous section, but to build a drop generator with membrane emulsification or a microfluidic device in laboratory has same challenges. Initial investment and maintenance are necessary. The

motivation of this study is to build a crossflow-based drop generation method in easier way. The experimental conditions can be widely changed, and the parts of the generator can be replaced.

From the studies of the drop generation methods introduced above, it is clear that the shear force by the CP played important role in the pinch-off processes of drops [12, 21]. The shear force acting on the drops also can be applied by the rigid body motion of the rotating continuous phase. This study is about using the shear force from the rotational rigid body motion of CP to develop a drop generator with predictable D_{drop} . The D_{drop} prediction will be discussed based on the models from the previous section.

1.4.2 Working Principle

Figure 1-17 shows the principle of the rigid body motion driven drops generation system. The V_c is from CP with rigid body motion. When the radius of the rotational rigid body motion is large enough, the flow direction of CP can be considered as linear at the position where CP meet with DP. Similar with the design of membrane emulsification, the DP is injected into CP in Q_d at an angle θ . A needle was used to inject the DP through a tubing, and the θ value was vertical to the flow direction of the CP. In this research, $\theta = 90^\circ$.

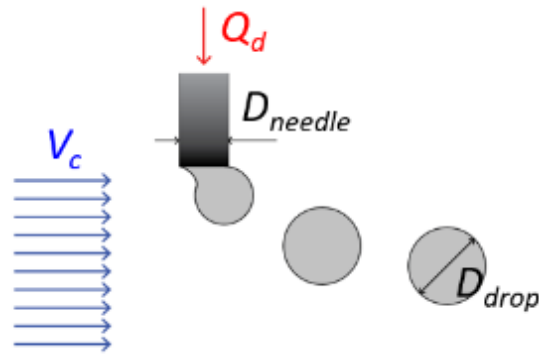


Figure 1-17. The principle of the rigid body motion driven drops generation system.

The schematic figure of the drop generation method based on rigid body motion was shown as Figure 1-18. The CP was filled a cylindrical container on a turntable. The rotating motion of turntable caused the rotational rigid body motion of the CP. The turntable was rotated by the AC/DC power supply. The DP was injected through a syringe needle by a syringe pump. The tip of the syringe needle was perpendicularly emerged under the free surface of the CP. Drops detached from the needle tip were carried by the rotational motion of the CP. In the meantime, the drops were falling down because of the gravity effects.

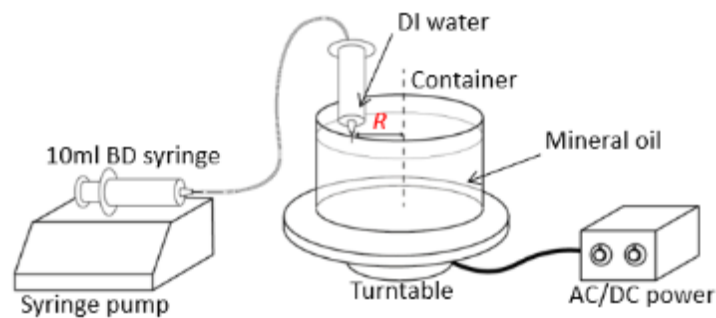


Figure 1-18. The schematic figure of the rigid body motion driven drops generation system.

Since it was possible to change the factors of the system independently, such as switching the rotating speed of the turntable or moving the position of the needle, the versatility of the system was high. Wide-ranging size of drops released from the system

was available based on controlling these key components [30]. Further analysis between the size of drop and each factor will be discussed based on the prototype of the system. As an example of application, hydrogel beads will be generated from the system, and the expansibility of the method will be considered.

Chapter 2 Methods and Materials

2.1 Materials

Mineral oil (Bluewater Chemgroup, 05089) and deionized water (DI water) were used as the CP and the DP, respectively. They were filtered to remove particles or dusts for better image quality. The properties of these two materials were measured as follows.

The density measurement was based on the Eq. (2-1).

$$\rho = \frac{m}{V}, \quad (2-1)$$

where m is the mass of the liquid sample, and V is the volume of the sample. A micropipette (Eppendorf Research plus) was used to transport 1000 μL liquid sample into a container on the electric weight (Scout Pro 400g). The mass of the liquid sample was read from the electric weight (Table 2-1), and then the density of the liquid sample was calculated. Measurement was repeated multiple times for each sample, and the averaged value of the calculated density was used.

Table 2-1 The measurement results of mass (unit: g).

Mineral oil	DI water
0.87	1.00
0.85	0.99
0.83	1.00
0.88	1.00
0.87	1.00
0.86	/
0.85	
0.87	
0.86	
0.86	
0.87	
Average values	
0.86	0.99

The viscosity measurement was done at 25 C° by using the rheometer (AR-1500EX) with a cone geometry (60 mm diameter, 1°) and flow sweep function. The gap between the geometry and the stage of the rheometer was filled with a measuring sample. The controlling software of rheometer, TRIOS, can read the resistant from the screw rod during rotating geometry. Figure 2-1 shows the viscosity measurement results. Both the CP (mineral oil) and the DP (DI water) showed Newtonian fluid behaviors, because the viscosities of the working fluids were constant in a wide shear rate range.

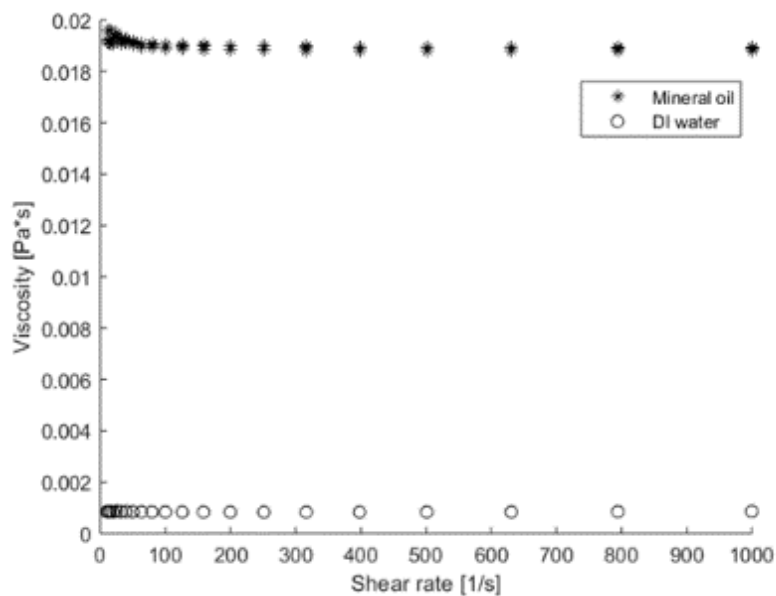


Figure 2-1. The viscosity measurement results of the rheometer.

The interfacial surface tension coefficient between the two liquids was measured based on the pendant drop method [52-55] using a goniometer (Attension Theta Goniometer). All of the measurements were operated at 22 C°, the room temperature. A glass container filled with CP (mineral oil) was placed on the stage of the goniometer. A DP (DI water) drop was formed in the oil using a syringe needle. The goniometer captured the growth of the water drop and measured the surface tension coefficient by processing the drop images. Based on the balanced forces acting on the drop, the

interfacial tension between DI water and mineral oil was calculated automatically by the goniometer. Figure 2-2 shows the surface tension coefficient measurement results. Most of the points with different volumes can be fitting on one single flat line. It means that the surface tension coefficient between the mineral oil and the DI water is constant for various sized drops. The outliers on the figure are caused by the reading error of the goniometer during the image processing, so they can be ignored.

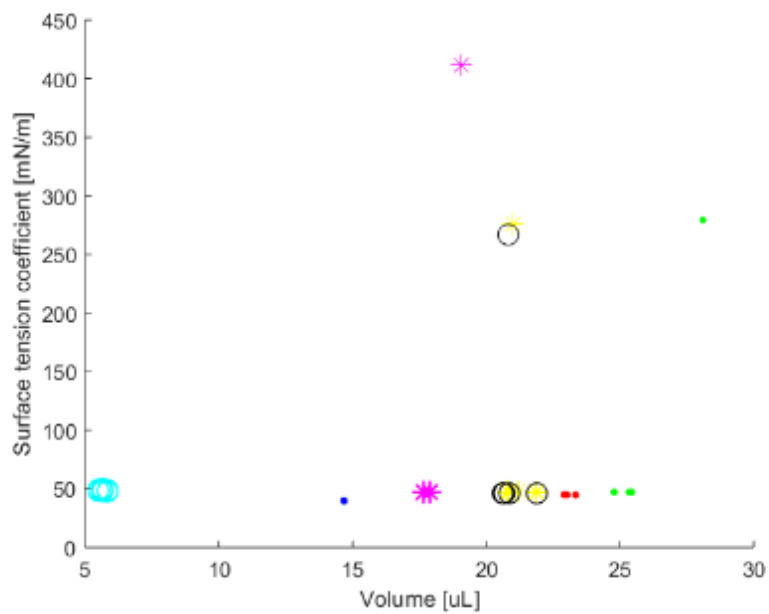


Figure 2-2. The interfacial surface tension coefficient measurement results of the goniometer.

The measured fluid property values are summarized in Table 2-2.

Table 2-2. The measured properties of the CP and the DP.

	DI water	Mineral oil
Density ρ [kg/m ³]	998	860
Viscosity μ [mPa·s]	0.85	19.00
Surface tension σ [mN/m]	45	

2.2 Experimental Setup

As Figure 2-3 shows, the experimental setup was built on an optical table. A 22 cm diameter cylindrical transparent container (Imagitarium, Freshwater Aquarium, 2.2 gallon) was placed on a turntable (Pioneer Belt Drive Stereo Turntable, PL-112D) to be used as the reservoir for the CP. The centers of the container and the turntable were carefully aligned. The turntable could rotate the CP in the container in rigid body motion at two different rotating speeds: $\Omega = 33.5$ and 45.1 rounds per minute (rpm), which are 3.5 and 4.7 rad/s, respectively. The rotating speed was confirmed by a tachometer (DF 2234C+ Digital Photo Tachometer).

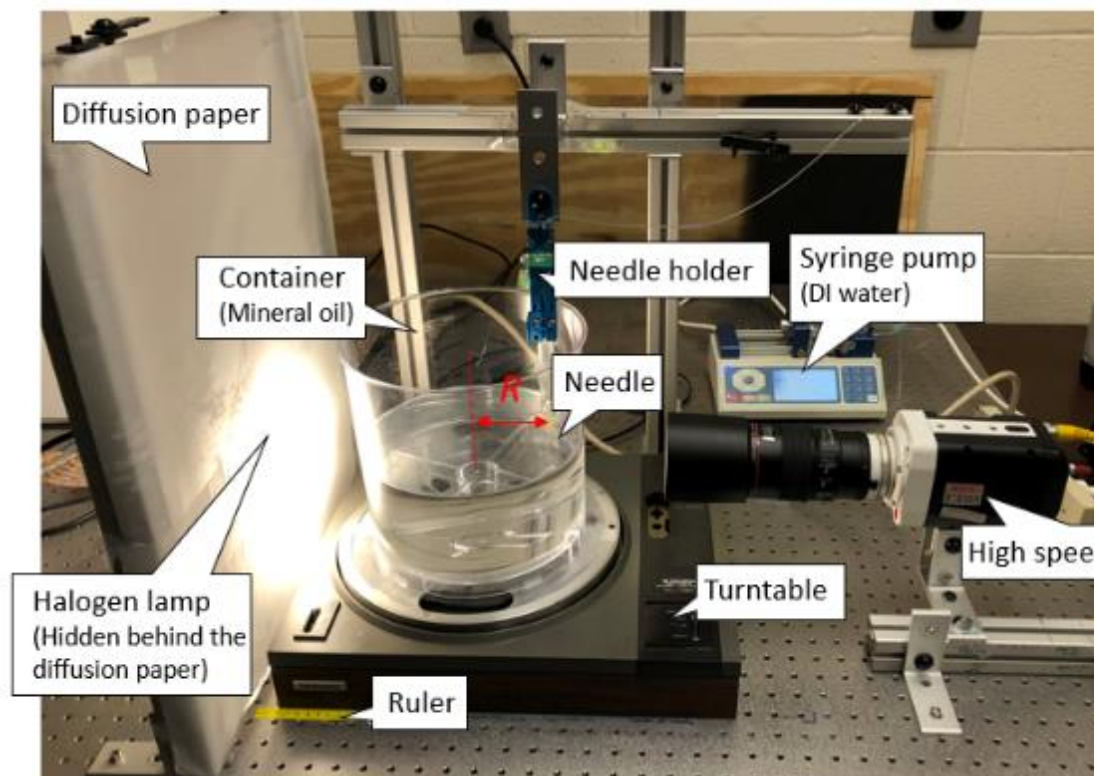


Figure 2-3. Experiment setup of drop generation.

The DP (DI water) was injected into the CP (mineral oil), through a syringe needle by a syringe (BD 10 mL plastic syringe) using a syringe pump (Fusion 200, Chemyx Inc). For different experimental conditions, the volume flow rate of the DP (Q_d) was applied at $Q_d = 0.1, 0.5, 1, 2, 4, 6, \text{ or } 8 \text{ mL/min}$. A tubing (Tygon tubing, Cole-Parmer, inner diameter: 0.020", outer diameter: 0.060") was used to deliver the DP from the syringe to the needle. At the end of the tubing, a customized needle holder (Mechanical parts, Makeblock) with a replaceable needle was fixed on a frame (OMA, McMaster-Carr) standing on the optical table. Water levels were used to check the horizontality and verticality of the needle holder.

Two kinds of 0.5"-long needle blunts with different inner diameters were used: SAI 23G needle (inner diameter: 0.0125", outer diameter: 0.025") or SAI 30G needle (inner diameter: 0.0055", outer diameter: 0.012" (SAI Infusion Technologies). The inner diameters of the needles, D_{needle} , was converted to 0.14 mm and 0.32 mm, respectively. The needle tip was submerged 8 to 10 mm below the free surface of the CP to reduce the disturbance from the needle hub. The linear velocity of the DP (V_d) was calculated from Q_d and D_{needle} ($V_d = \frac{Q_d}{\frac{\pi D_{needle}^2}{4}}$). The tubing from syringe pump was inserted inside the needle holder.

A reference ruler (Peel n Stick Removable Ruler Tape, Thermoweb) fixed on the optical table was used to determine the position of the turntable. The distance from the needle to the container center (i.e., the axis of rotation) (R) was adjusted to 40, 60, and 80 mm by moving the turntable back and forth with respect to the reference ruler. Thus, the linear velocity of the CP at the needle tip (V_c) could be controlled by changing either

the distance or the needle-to-container-center rotating speed of the turntable ($V_c = R \cdot \Omega$). A high-speed camera (MIRO M310, Vision Research, Phantom) with a macro lens (Canon, 100 mm, f1.x) was used to capture drop generation. The distance from the lens to the needle holder was about 90 mm. For better imaging of the drop generation processes, the camera was aligned on the line passing through the center of the container and the needle, and the container was illuminated by a halogen lamp through a diffusion paper. For consistent focusing, the relative positions between the needle and the camera was fixed.

In summary, the established experimental setup enabled examining the drop generation processes with various D_{needle} , V_c , and Q_d . Applied experimental conditions are summarized in Table 2-3.

Table 2-3. The experimental conditions applied for the drop generation processes.

D_{needle} [mm]	0.14				0.32		
Q_d [mL/min]	0.1	0.5	1	2	4	6	8
R [mm]	40		60			80	
Ω [rad/s]	3.5				4.7		

The experimental conditions were converted to V_c and V_d as shown in Table 2-3 and 2-4.

Table 2-4. V_c values [mm/s] calculated from the experimental conditions.

		Ω [rad/s]	
		3.5	4.7
R [mm]	40	140.3	189.0
	60	210.4	283.6
	80	280.6	378.1

Table 2-5. V_d values [mm/s] calculated from the experimental conditions.

		D_{needle} [mm]	
		0.14	0.32
Q_d [mL/min]	0.1	108.7	21.1
	0.5	543.7	105.3
	1	1087.3	210.5
	2	2174.7	421.0
	4		842.0
	6		1263.1
	8		1684.1

2.3 Experimental Procedures

Drop generation processes were investigated with the multiple experimental conditions as shown in the previous section. For each condition, the turntable was moved to the desired position of the R value with the container filled with the CP.

The next step was to prepare high-speed imaging. For most of the experiment, the setting of the high-speed camera was 400 fps and 200 μ s for the frame rate and exposure time, respectively. The frame rate was adjusted to 40 fps for slow drop generation processes with low Q_d . The aperture number of the macro lens was set to 11-15 for varies distances between the needle tip and the camera lens.

It was found that the cylindrical container distorted drop images due to its curved surface. A reference image of a grid plate at chosen R was captured for image correction before recording the drop generation processes. As Figure 2-4 shows, the grid plate was placed at the position of the needle by a customized frame (Mechanical parts, Makeblock). The grid plate was made by gluing a transparency film (APOLLO Laser Printer Transparency Film) with printed 5 mm \times 5 mm square grid patterns on a slide glass (75 mm \times 50 mm \times 1.0 mm, Fisherbrand Plain Microscope Slides). A picture of the grid plate was taken as Figure 2-5 shows to be used for the image process step later on.

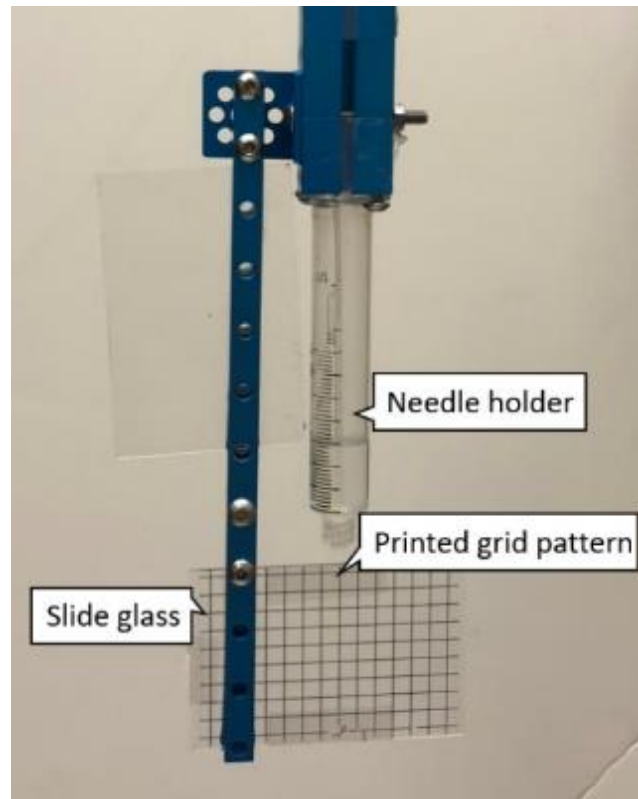


Figure 2-4. The grid plate attached on the needle holder for image correction.

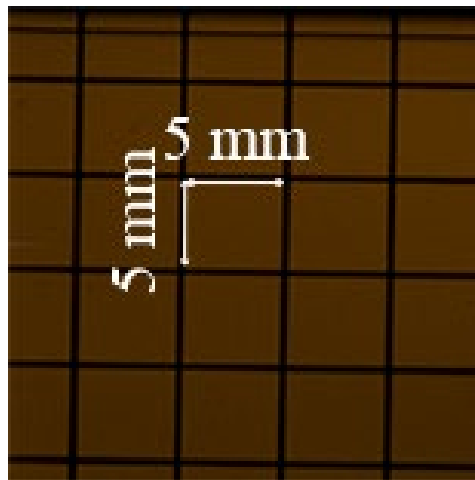


Figure 2-5. A reference image of the grid plate in the continuous phase.

After reference image taking, the grid plate was replaced with the syringe of the chosen D_{needle} , and the turntable was set to the determined rotating speed Ω . The syringe was filled with degassed DI water and connected to the needle holder via the tubing. The syringe was placed on the syringe pump, and the determined Q_d was input to the

syringe pump. After these steps to set the running conditions to desired values, the preparation step of the experiment was finished.

For the experimental process, the turntable was turned on first. The selected rotating speed could be achieved after 1- 2 rotations. Then the syringe pump was turned on to inject the DP at chosen Q_d . Several seconds were needed for the syringe pump to reach the set value of Q_d . After the steady generation of drops was observed, the process was captured using the high-speed camera. Videos without undesired objects, such as air bubbles remaining in the DP, were saved for processing.

The afore mentioned steps were repeated for different conditions.

2.4 Image Correction

The reason for having reference images of the grid plate was that the drops in the captured images appeared to be stretched in the horizontal direction. Thus, the drops seemed to be an ellipsoid, not a sphere as Figure 2-6 shows. This aspect ratio change of the drop image was caused by the cylindrical wall of the container filled, which played a role as a cylindrical lens. Therefore, it was required to calibrate the aspect ratio change of the obtained images and to re-scale the images.

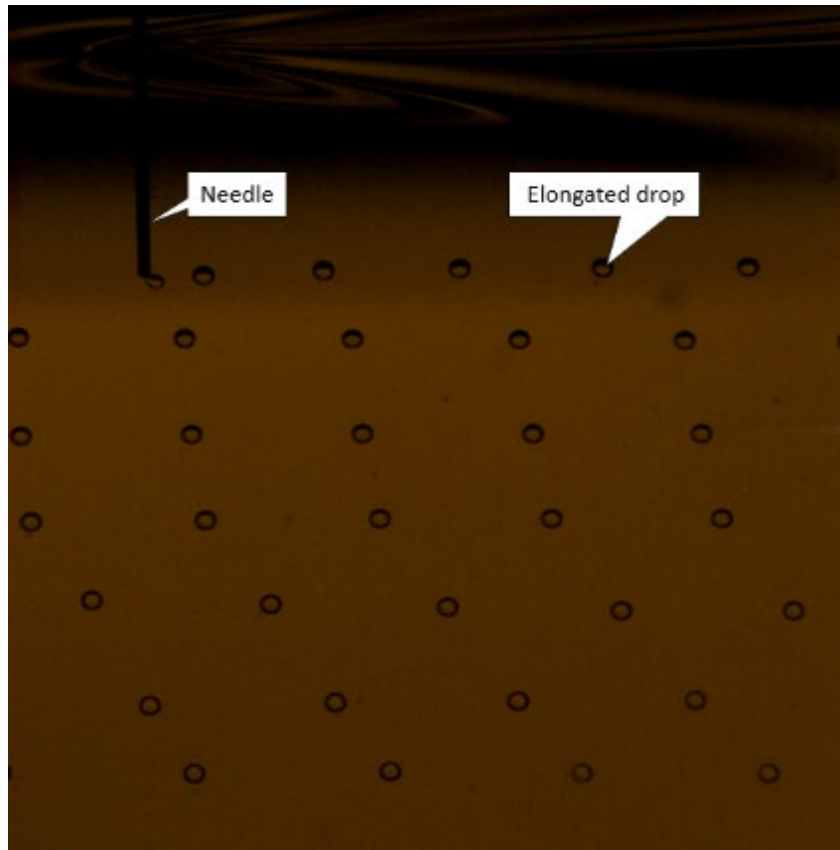


Figure 2-6. A raw image of drop generation processes ($R = 80 \text{ mm}$, $\Omega = 4.7 \text{ rad/s}$, and $Q_d = 0.5 \text{ mL/min.}$).

The reference images of the grid plate were used to calculate the elongated aspect ratio. The reference images were read into ImageJ [56, 57] to measure the x and y coordinates of intersection points of the grid. The coordinates were digitized from the image. The brightness and contrast of the image were adjusted to identify the positions of intersection points. For the purpose of convenience, the intersection points were named as shown in Figure 2-7.

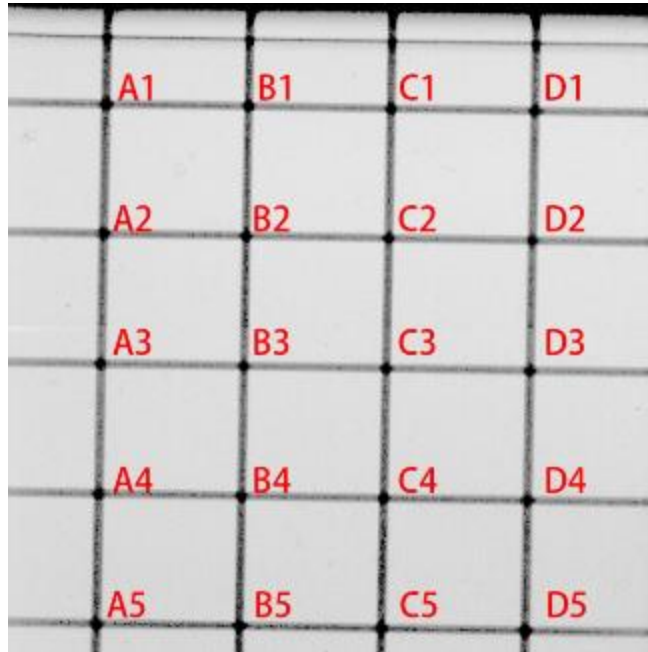


Figure 2-7. The x and y coordinates measurements of the intersection points from the reference image.

Matlab (The MathWorks, Inc.,) was used for the following analysis of the measured coordinates. According to the design of the printed patterns and the experimental setup, the lines A1-D1, A2-D2, A3-D3, A4-D4, and A5-D5 should be horizontal, and the lines A1-A5, B1-B5, C1-C5, and D1-D5 should be vertical in the image. The slopes of these lines were calculated based on the trigonometric functions from measured coordinates and converted to angles. To find the tilted angle of the recorded images (α), the angle differences between the grid lines and the horizontal and vertical directions were calculated and averaged as α .

Similarly, the x - y aspect ratios of the images were calculated from the measured coordinates of the grid. Since grid shapes were square, the vertical segments from this image should be same. The length of each segment was calculated, and then the aspect ratio of the images (AR) was calculated as the ratio of the average length of vertical

segments to that horizontal segments.

The intersection coordinates, α , and AR , were measured for every reference image. The results are summarized in Table 2-6. α and AR were used to correct the recorded images using ImageJ. A cropped image from Figure 2-6 is shown in Figure 2-8 as an example. The α and AR were calculated as 1.08° and 0.91, respectively. The image was imported into ImageJ, and then rotated and rescaled. The corrected image is shown in Figure 2-9. Compared with the raw image, the drops in the adjusted image look spherical.

Table 2-6. The calculation results of tilted angles and elongated aspect ratios.

		D_{needle} [mm]	
		0.14	0.32
R [mm]	40	$\alpha = 0.72^\circ, AR = 0.82$	$\alpha = 1.14^\circ, AR = 0.82$
	60	$\alpha = 0.31^\circ, AR = 0.86$	$\alpha = 0.90^\circ, AR = 0.86$
	80	$\alpha = 1.08^\circ, AR = 0.91$	$\alpha = 0.74^\circ, AR = 0.90$



Figure 2-8. A cropped raw image of drop generation processes.



Figure 2-9. An adjusted image of drop generation processes.

2.5 Image Processing of Drops

Automated droplet measurement (ADM), image processing software for drop generation [58, 59] was used to process drop images and to measure the sizes of drops. The interface and working processes of ADM are shown in Figure 2-10.

After the recorded images were loaded into ADM, the unit conversion columns (' $\mu\text{m}/\text{pixel}$ ' and 'frame/second') had to be filled. The ' $\mu\text{m}/\text{pixel}$ ' was the pixel scale used to convert the pixel-based dimension in the image to the real unit. The outer diameters of the two used needles ($D_{\text{needle}} = 0.14 \text{ mm}$ and 0.32 mm) were 0.30 mm and 0.64 mm , respectively, and they were compared with the measured number of pixels across the needles in ImageJ to calculate the pixel size as Table 2-7 shows. The 'frame/second' was filled with the corresponding values of the high-speed camera.

Table 2-7. Pixel size for different experimental conditions.

D_{needle} [mm]	R [mm]	$\mu\text{m}/\text{pixel}$
0.14	40	26.1
	60	27.3
	80	28.6
0.32	40	29.2
	60	29.4
	80	31.4

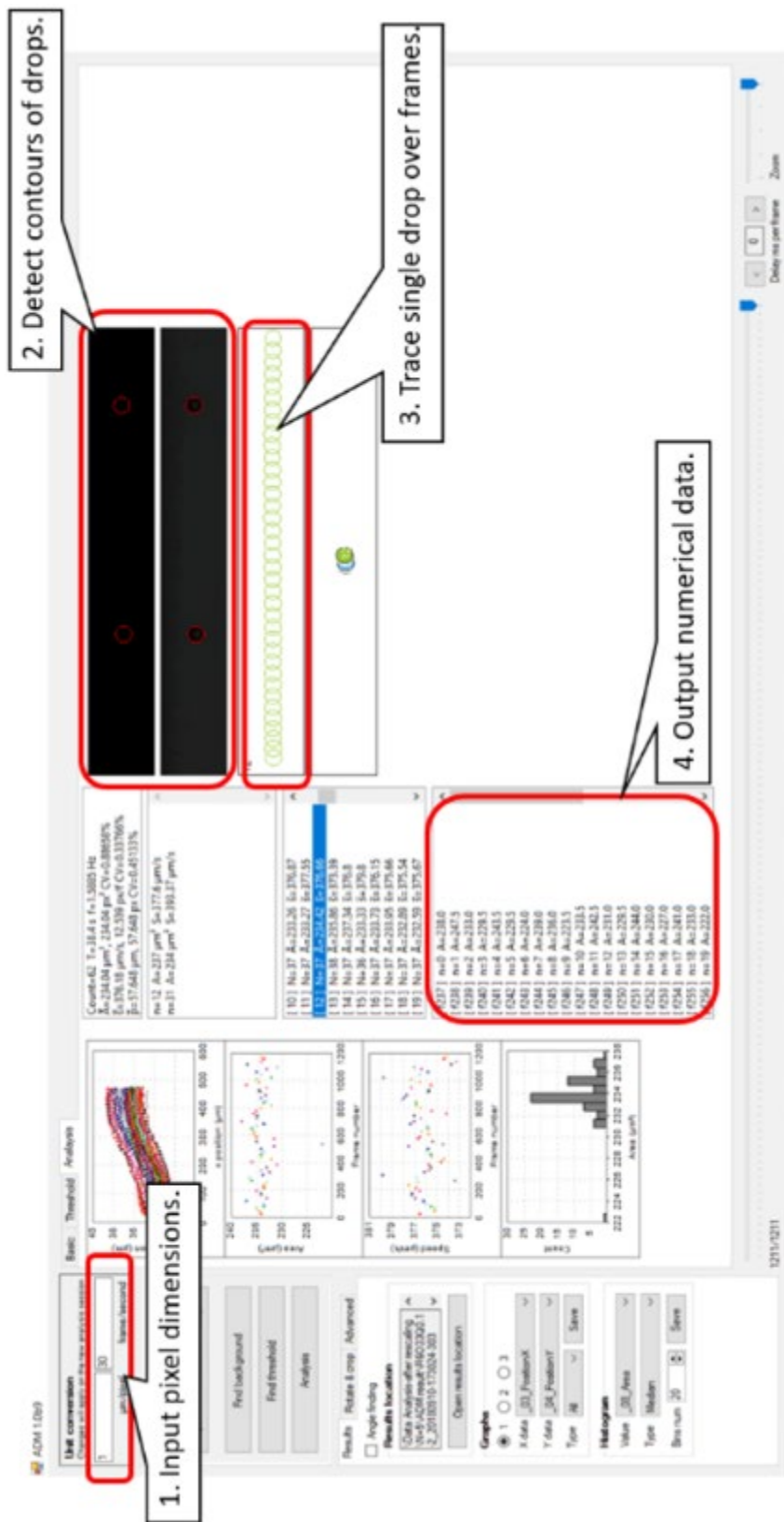


Figure 2-10. The measurement processes of drops in the ADM [58, 59].

ADM compared every frame of the drop generation processes to automatically extract a constant background image. The image with the background removed was used for the following steps of the processing. The optimum image intensity value for drop detection was determined by ADM's binary threshold value finding function. Then, ADM could detect the contours of drops from images. A single drop was traced over frames, and its size was recorded for each frame. As a result, the diameters of multiple drops were collected for this study. For each experimental condition, more than one hundred drops were recorded ($N > 100$).

Chapter 3 Results

As briefly shown in the previous chapter, DI water drops were generated from the needle tip with the rigid body rotation of the mineral oil in the container. This result justifies the assumption that the rigid body motion of the CP created shear force to separate drops from the vertically injected DP. Multiple spherical drops with similar diameters were continuously released from the needle tip. It was observed that the drops generation process achieved steady state. The diameter of the generated drops could be controlled by adjusting the velocities of the CP and the DP, V_c and V_d .

3.1 Experimental Images and Drop Pinch-off Modes of the Drops

The pinch-off modes of generated drops were different depending on experimental conditions. The drop generation modes in cross-flow are classified as the squeezing, dripping, and jetting mode [2]. The squeezing mode, which can occur in microfluidic drop generators, was not observed in this study [36]. The other two modes were observed with different experimental conditions.

Figures 3-1 and 3-2 show the examples of the two drop generation modes. The experimental conditions were $D_{needle} = 0.14$ mm, $V_c = 210.4$ mm/s and $V_d = 543.7$ mm/s, and $V_c = 210.4$ mm/s and $V_d = 2174.7$ mm/s, respectively.

In Figure 3-1, the pinch-off occurred at the needle tip, which is recognized as the dripping mode. In Figure 3-2, it is clear that the distance from the needle tip to the

pinch-off location exceeded D_{drop} ($L > D_{drop}$) [38]. Therefore, it was observed that changing V_d only can cause change in the pinch-off mode.



Figure 3-1. The drop generation process of $V_c = 210.42$ mm/s, and $V_d = 543.67$ mm/s.

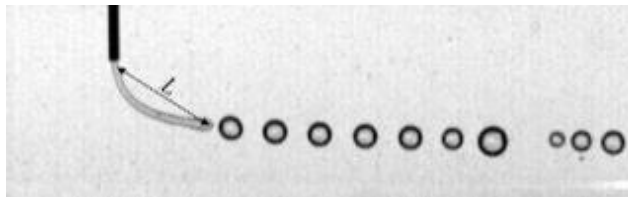
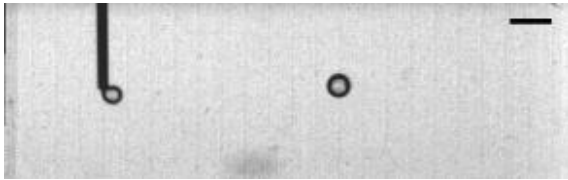
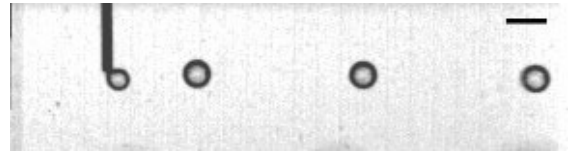
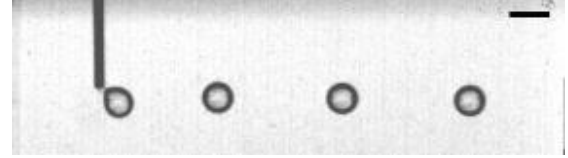
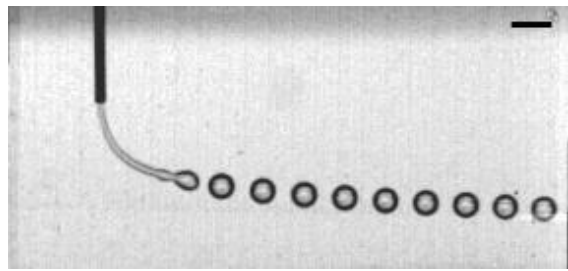


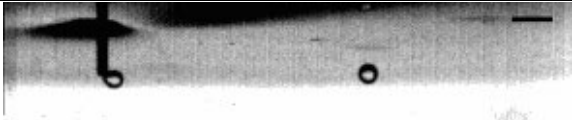

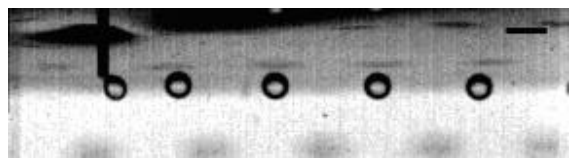
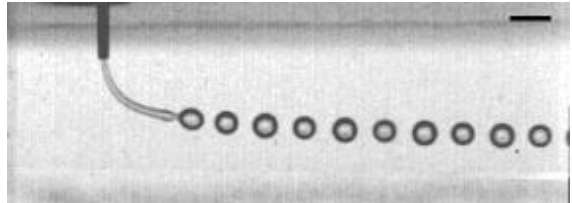

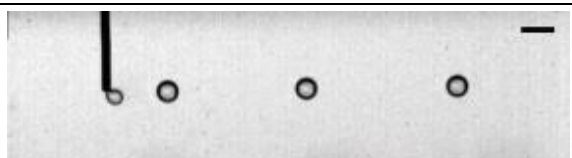
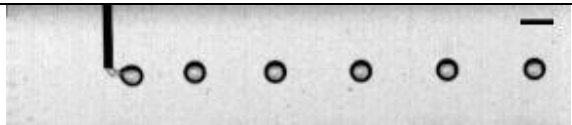
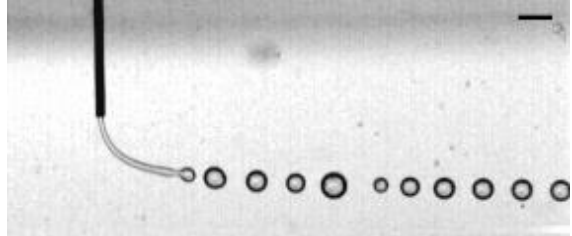
Figure 3-2. The drop generation process of $V_c = 210.42$ mm/s, and $V_d = 2174.68$ mm/s.

Based on the definitions of the modes, it was possible to distinguish the pinch-off modes for all cases. By summarizing the results, the images with varies V_c and V_d were illustrated as Table 3-1 and 3-2.

Table 3-1. Drop generations with $D_{needle} = 0.14$ mm (scale bar = 1 mm).

V_c [mm/s]	V_d [mm/s]	Image	Mode
140.28	108.73		Dripping
	543.67		Dripping
	1087.34		Dripping
	2174.68		Jetting

(Continued)

V_c [mm/s]	V_d [mm/s]	Image	Mode
189.04	108.73		Dripping
	543.67		Dripping
	1087.34		Dripping
	2174.68		Jetting
210.42	108.73		Dripping
	543.67		Dripping
	1087.34		Dripping
	2174.68		Jetting

(Continued)






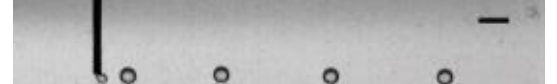



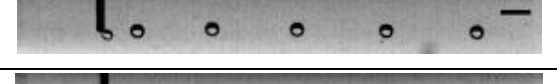

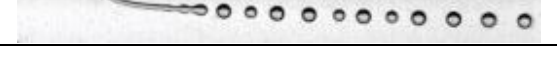

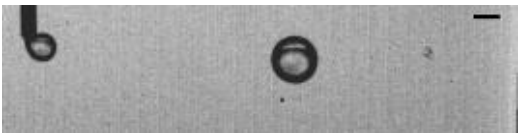

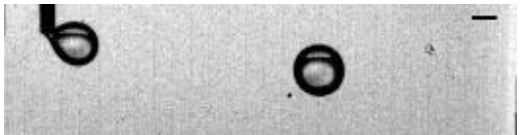

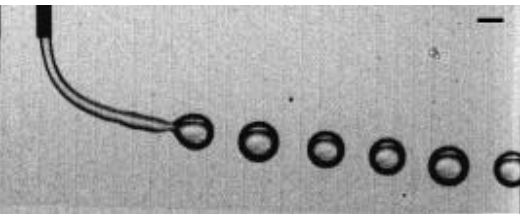
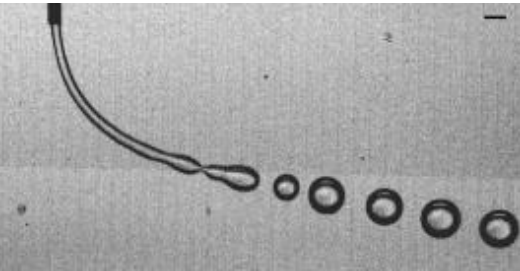

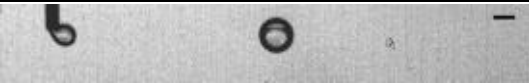
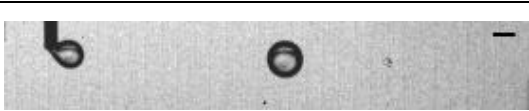

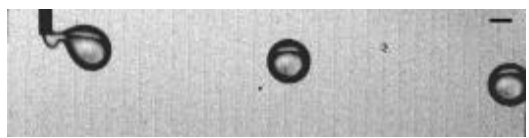
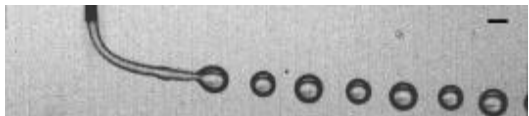
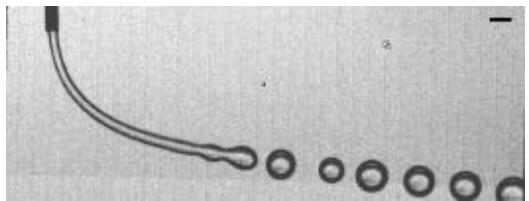
V_c [mm/s]	V_d [mm/s]	Image	Mode
283.56	108.73		Dripping
	543.67		Dripping
	1087.34		Dripping
	2174.68		Jetting
280.57	108.73		Dripping
	543.67		Dripping
	1087.34		Dripping
	2174.68		Jetting
378.08	108.73		Dripping
	543.67		Dripping
	1087.34		Dripping
	2174.68		Jetting



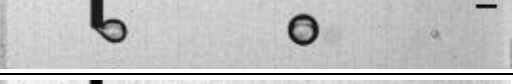

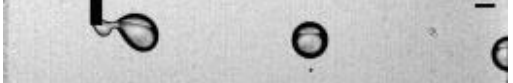
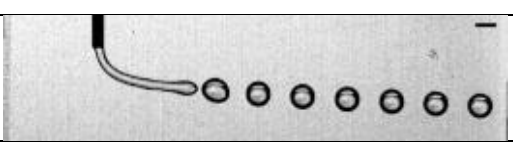
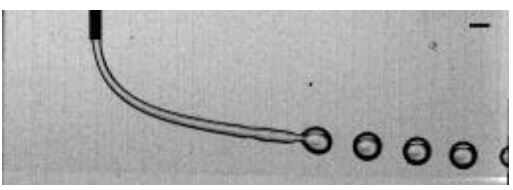
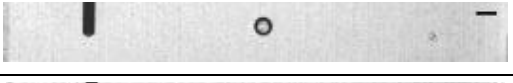


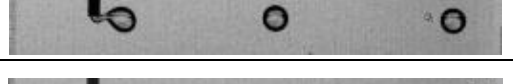

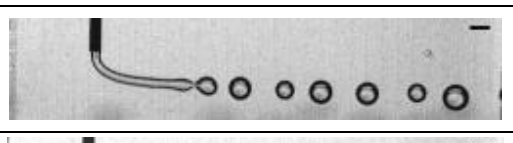
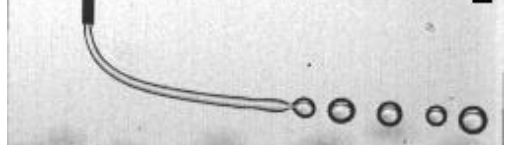
Table 3-2. Drop generations with $D_{needle} = 0.32$ mm (scale bar = 1 mm).

V_c [mm/s]	V_d [mm/s]	Image	Mode
140.28	21.05		Dripping
	105.26		Dripping
	210.51		Dripping
	421.02		Dripping
	842.04		Dripping
	1263.06		Jetting
	1684.08		Jetting




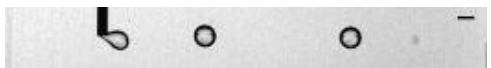

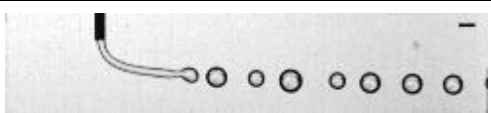
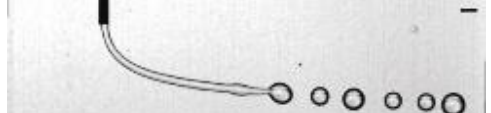




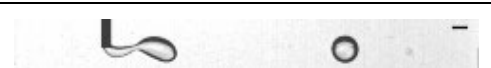
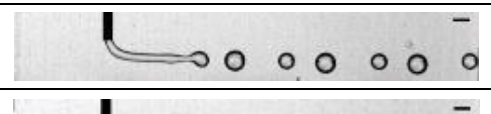
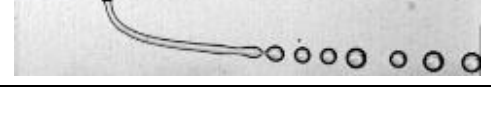
(Continued)

V_c [mm/s]	V_d [mm/s]	Image	Mode
189.04	21.05		Dripping
	105.26		Dripping
	210.51		Dripping
	421.02		Dripping
	842.04		Dripping
	1263.06		Jetting
	1684.08		Jetting

(Continued)

V_c [mm/s]	V_d [mm/s]	Image	Mode
210.42	21.05		Dripping
	105.26		Dripping
	210.51		Dripping
	421.02		Dripping
	842.04		Dripping
	1263.06		Jetting
	1684.08		Jetting
283.56	21.05		Dripping
	105.26		Dripping
	210.51		Dripping
	421.02		Dripping
	842.04		Dripping
	1263.06		Jetting
	1684.08		Jetting

(Continued)

V_c [mm/s]	V_d [mm/s]	Image	Mode
280.57	21.05		Dripping
	105.26		Dripping
	210.51		Dripping
	421.02		Dripping
	842.04		Dripping
	1263.06		Jetting
	1684.08		Jetting
378.08	21.05		Dripping
	105.26		Dripping
	210.51		Dripping
	421.02		Dripping
	842.04		Dripping
	1263.06		Jetting
	1684.08		Jetting

3.2 Drop Diameter Distribution

As introduced in the previous section, the diameters of generated drops (D_{drop}) were automatically measured using ADM. The average and standard deviation values of D_{drop} with various combinations of V_c and V_d are summarized in Table A-1. Because of the low frequency of drops generations, the ADM analysis of the images from $V_c = 140.28$ mm/s, $V_d = 21.05$ mm/s and $V_c = 189.04$ mm/s, $V_d = 21.05$ mm/s was not able to be produced.

Because the goal of this study is to generate monodisperse drops continuously, it is important to narrow down the range of the D_{drop} to certain experimental conditions. For this purpose, the histograms of drops sizes were plotted using the measured D_{drops} [60].

Figure 3-3 shows an example of the histogram to compare drop size distributions between two different V_c values ($V_c = 140.3$ mm/s: blue, and 189.0 mm/s: red) with same $V_d = 543.7$ mm/s, and $D_{needle} = 0.14$ mm. The x-axis was the range of D_{drop} . For $D_{needle} = 0.14$ mm experiments, the interval was chosen as $2 \mu\text{m}$ to have the optimum view of the plots. The y-axis was the probabilities of each range of the diameter values. With these conditions, drops were generated in the dripping mode. Accordingly, the histogram shows narrow drop size distribution with only one peak for each case. Therefore, the generated drops in the experimental conditions were well controlled.

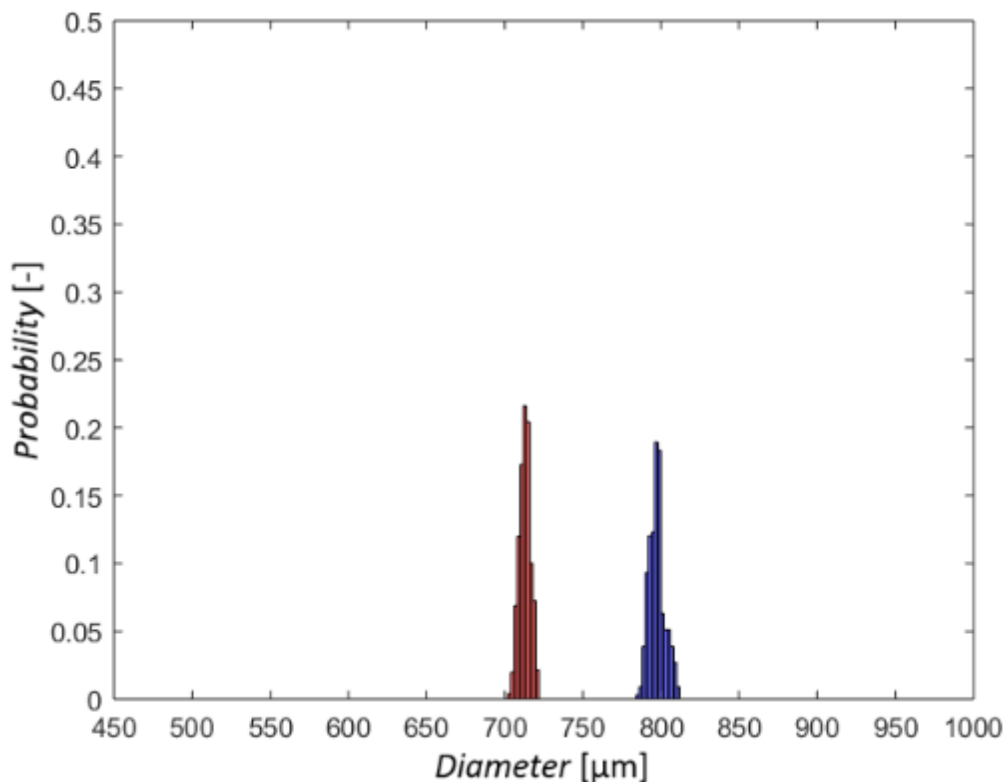


Figure 3-3. Drop size distribution of $V_c = 140.3$ mm/s or 189.0 mm/s, $V_d = 543.7$ mm/s,

$$D_{needle} = 0.14 \text{ mm.}$$

Figure 3-4 shows another example: $V_c = 140.3$ mm/s (blue) or 189.0 mm/s (red), $V_d = 2174.7$ mm/s, and $D_{needle} = 0.14$ mm. As shown previously, higher Q_d was applied for these experimental conditions (i.e., higher V_d), the pinch-off mode was the jetting mode.

Compared with Figure 3-3, the most significant difference found in Figure 3-4 is the number of the peaks. In contrast to on single sharp peak of the dripping mode, multiple peaks are found in the jetting mode. This appears to be due to the Rayleigh-Plateau instability which causes pinch-off in the jetting mode. As the jet stream of the DP got longer, surface tension developed this wavy instability. Thus, the pinch-off occurring at the stream tip more randomly, which resulted in multiple peaks [12].

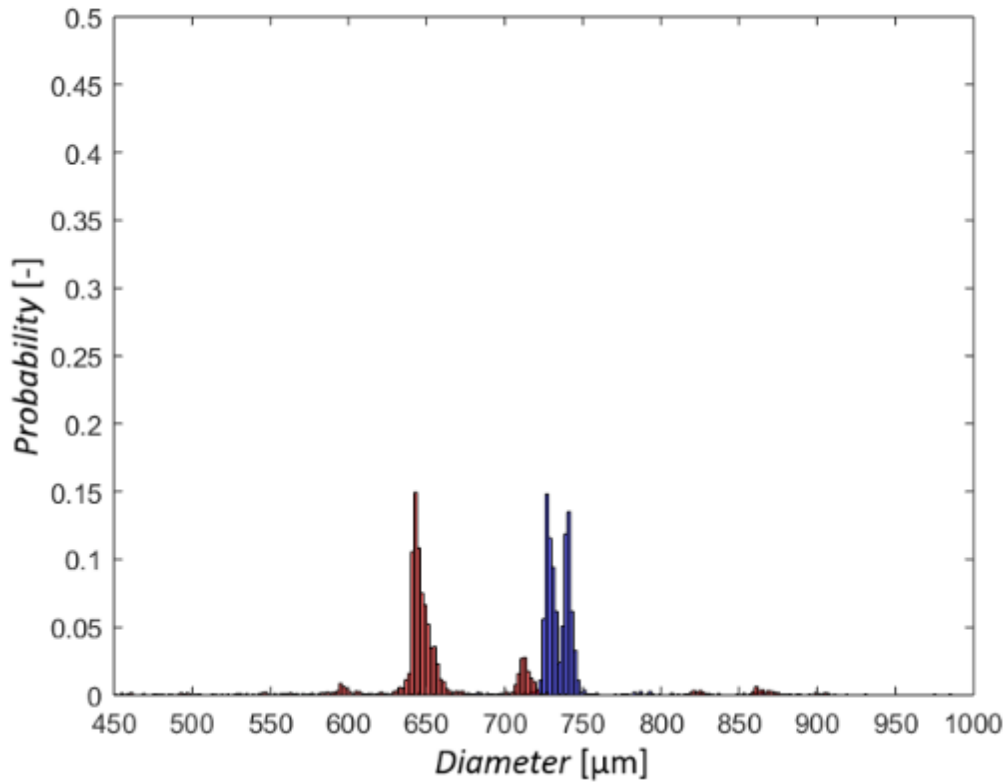


Figure 3-4. The histograms of $V_c = 140.28 \text{ mm/s}$ or 189.04 mm/s , $V_d = 2174.68 \text{ mm/s}$,

$$D_{\text{needle}} = 0.14 \text{ mm}.$$

All histograms of $D_{\text{needle}} = 0.14 \text{ mm}$ and 0.32 mm are shown in Table B-1 and B-2, respectively. As references, the pinch-off modes are noticed in the tables.

The coefficient of variation (CV) of drop size was used to evaluate the monodispersity of generated drops based on the Eq. (3-1), (3-2), and (3-3) [2, 24].

$$\text{Standard deviation of } D_{\text{drop}}: \text{STD}_{D_{\text{drop}}} = \sqrt{\frac{1}{n} \sum_{i=1}^n (D_{\text{drop},i} - \overline{D_{\text{drop}}})^2}, \quad (3-1)$$

$$\text{Mean of } D_{\text{drop}}: \overline{D_{\text{drop}}} = \frac{1}{n} \sum_{i=1}^n D_{\text{drop},i}, \quad (3-2)$$

$$\text{CV} [\%] = \frac{\text{STD}_{D_{\text{drop}}}}{\overline{D_{\text{drop}}}} \times 100, \quad (3-3)$$

The values of CV were calculated for each experimental condition individually.

The detailed calculated results of CV are shown in Table B-3. The generated drops showed different ranges of CV in the dripping mode and in the jetting mode as $0.21 \sim$

6.8 % and 1.1 ~ 14.9 %, respectively. Because polydispersed drops were generated in the jetting mode, the values of CV in the jetting mode are higher than the values in the dripping mode.

Table 3-3 is the comparison of the monodispersity of generated drops between different methods. The values of CV in this study are higher than using crossflow-based microfluidic device, but lower than using membrane emulsification. Thus, the monodispersity of generated drops using this method is acceptable in the comparison.

Table 3-3. The comparison of drop monodispersity between different methods.

Method	CV [%]
The method in this study	Dripping mode: 0.21 ~ 6.8
	Jetting mode: 1.1 ~ 14.9
Crossflow-based microfluidic device	< 2 [61]
Step emulsification	< 1 [62]
Microchannel emulsification	< 5 [63]
Membrane emulsification	~ 20 [64]

3.3 Dimensionless Phase Diagram of the Drop Generation

It is useful to present the obtained data in a dimensionless map for predicting drop generation mode and size [36]. As such V_d/V_c and D_{drop}/D_{needle} are natural choices for plotting a dimensionless map of this study. The numeric values of V_d/V_c and D_{drop}/D_{needle} are summarized in Table C-1.

A dimensionless map for $D_{needle} = 0.14$ mm is shown in Figure 3-5. Based on the discussion in the previous sections, drops in different pinch-off modes were indicated in the map with different markers as the legends of Figure 3-5 shown. Different markers were used as the figure shown. The hollow markers and the solid markers were indicating the dripping mode zone and the jetting mode zone, respectively.

3.4 The Different Pinch-off Zones in the Nondimensional Analysis Phase Diagram

In Figure 3-5, it was possible to separate the map as two zones, the dripping mode zone and the jetting mode zone. The markers with the same colors were indicating the same values of Q_d . Boundaries of each zone were identified by connecting these markers as straight lines. As Figure 3-6 shows, the hollow markers and the solid markers indicated the pinch-off modes of drops as the dripping mode and the jetting mode, respectively. A boundary between these two zones as the DJT was not identified in current experiments. It will be a part of the future work of this study.

From the map, it was clear that for higher V_d , the ratio of D_{drop} and D_{needle} was increased. If the same needles were used, D_{drop} was increasing with V_d in the dripping mode zone. If the V_d was higher than the criteria value, the pinch-off mode became the jetting mode. The ratio of D_{drop} and D_{needle} was slightly decreased for the experimental conditions with fixed V_c . By knowing the experimental conditions, the pinch-off zone of drop generation processes in the map was predictable.

Mode	
Hollow marks	Dripping
Solid marks	Jetting
V_c [mm/s]	
○	138.2
☆	188.4
□	207.3
▽	276.4
◇	282.7
△	376.9
D_{nozzle} (inner diameter) [mm]	
Small marks	0.14
Big marks	0.32
Q_d [mL/min]	
Red	0.1
Green	0.5
Blue	1
Black	2
Yellow	4
Cyan	6
Magenta	8

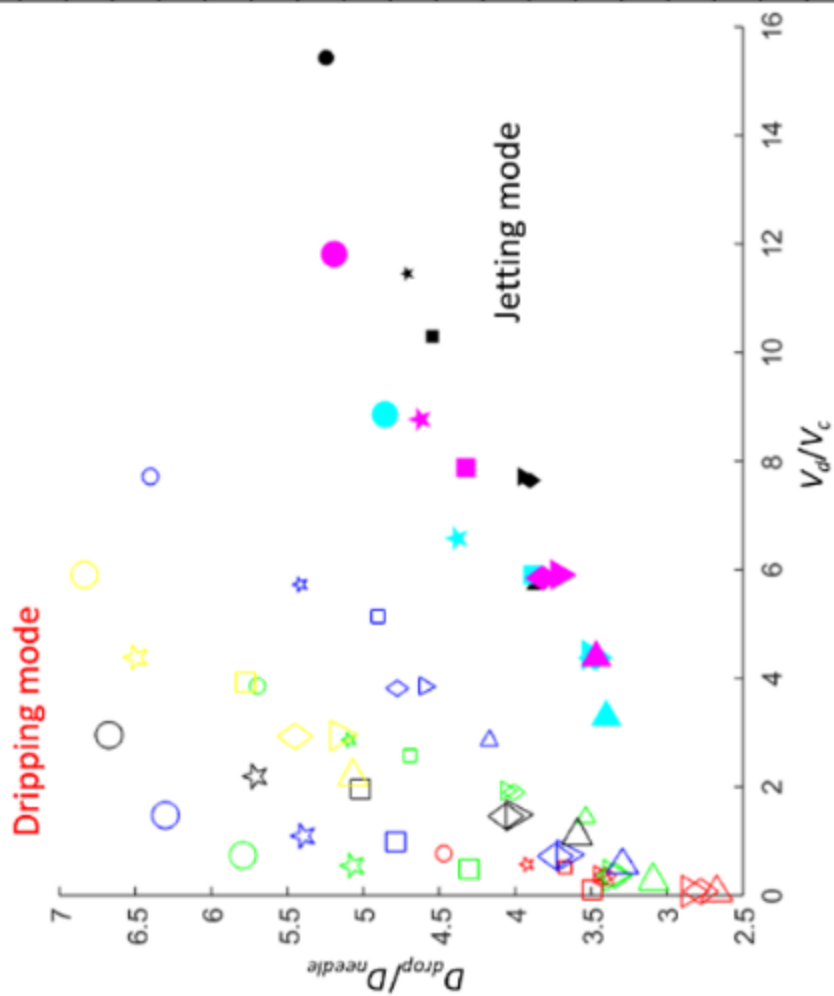


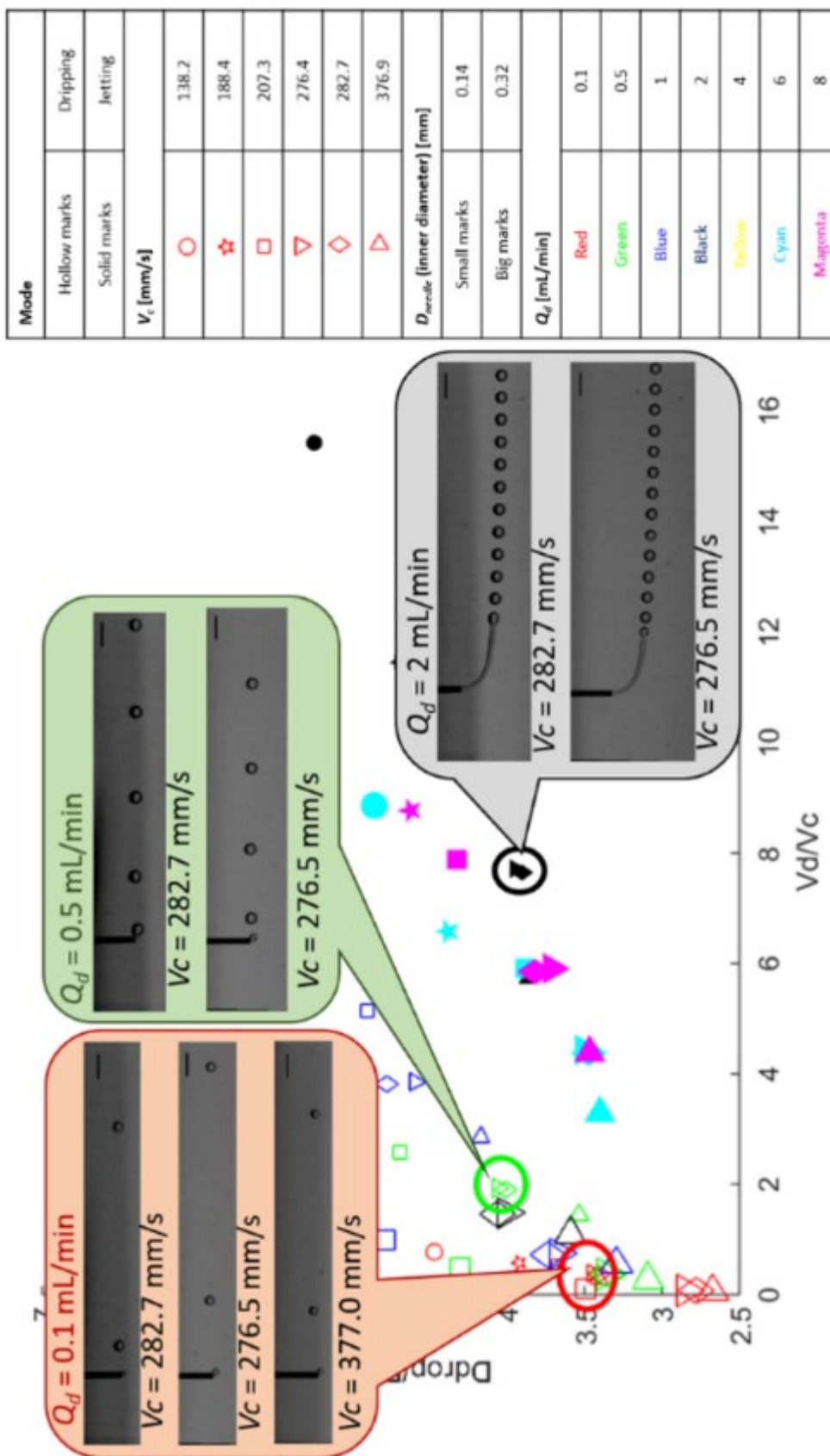
Figure 3-6. The zones of pinch-off modes in the nondimensional analysis phase diagram.

3.5 The Application of the Nondimensional Analysis Phase Diagram

The map was supposed to be a reference of drop size predictions. For different experimental conditions, if the coordinates of the data were closed to each other in the map, the pinch-off processes and the diameters of the drops should be similar.

Figure 3-7 was an example of the predictions of the drop generations. 3 different positions on the map were chosen. The images of the drop generation processes closed to the positions were illustrated for comparison. The experimental conditions for each image were included in the map. As the figure shown, the products of drops were similar, even the experimental conditions for the drop generations were different.

In this map, data points in the jetting mode are in one line with narrow range. It is possible to predict D_{drop} easily with known experimental conditions if the pinch-off mode of drop generation is jetting mode. But the prediction does not work well for drops in the dripping mode because of the widely range of data points in the dripping mode zone. Currently, the data points in the dripping mode zone can be used as references of produced D_{drop} with same experimental condition. For the purpose of predicting D_{drop} with arbitrary experimental conditions, building scaling laws will be considered as future works.



Mode	
Hollow marks	Dripping
Solid marks	Jetting
V_c [mm/s]	
○	138.2
☆	188.4
□	207.3
▽	276.4
◇	282.7
△	376.9
D_{needle} (inner diameter) [mm]	
Small marks	0.14
Big marks	0.32
Q_d [mL/min]	
Red	0.1
Green	0.5
Blue	1
Black	2
Yellow	4
Cyan	6
Magenta	8

Figure 3-7. The applications of the nondimensional analysis phase diagram.

Chapter 4 Discussion

4.1 Absence of the Squeezing Mode

In this study, only the dripping and jetting mode were observed whereas the squeezing mode was not. The absence of the squeezing mode can be explained as follows.

When the DP is injected into the T-junction device, the tip of the DP stream enters the junction and is elongated through the channel. Because the tip of the DP stream clogs the channel, pressures on each side of the stream are different. As the DP grows in the channel, the pressure difference also increases. Eventually, the pressure difference becomes large enough to break the DP stream into a drop confined by the channel wall. Therefore, the main factor of the squeezing mode in the T-junction device is the pressure difference, and the boundary walls of the microfluidic channel play critical roles to cause the clogging of the channel by the DP [36].

In the present study, however there was no surrounding geometry which could confine the flow of the DP. As a result, the squeezing mode did not occur in the current system.

4.2 Controlling Drop Diameter

In this study, it was possible to modulate drop sizes. It was clear that increase in V_c generated smaller drops in the dripping modes. This is because as V_c increased, drag on

the drop growing at the needle tip increased, which drives the pinch-off processes of drops. Also, the drops were allowed shorter time for the growth before pinch-off.

For the changing of V_d , D_{drop} increased when higher V_d was applied in the dripping modes. If the V_c was fixed, the allowed time of drop growth before pinch-off was the same. Higher V_d was able to apply more amount of the DP into the drop. In this case, D_{drop} had included more liquid than the drop can have with lower V_d , D_{drop} would be bigger.

As V_d increased, a neck could be observed between the needle tip and the generated drop, which indicates that the pinch-off mode was switching from the dripping mode to the jetting mode. Once V_d was high enough, the jetting mode became prevalent and D_{drop} had decreased compared with the dripping mode [21, 38, 42] .

In the jetting mode, instability developed along the elongated DP stream in the CP. Because of the significantly increased surface area and the tendency of the DP to minimize the surface area, unstable wavy shapes occur among the stream. Eventually, the tip of the stream was ruptured into drops. In the jetting mode, the shear force was not the main driving force of drop generations, and thus changing V_c could not change D_{drop} so much.

4.3 Nondimensional Numbers in the Drop Generation Processes

Nondimensional numbers, Ca and We , are also used to predict drop generation modes [21, 38, 42]. These numbers were calculated based on Eq. (1-1) and (1-2), and the numerical values are shown in Table D-1.

A dimensionless map of Ca and We is plotted in Figure 4-1. Here, the hollow and solid markers indicate the dripping and jetting mode, respectively. From the previous discussion, the jetting mode occurs for higher Ca and We . Because of the limited experimental data, the dependent with Ca and the DJT is not clear in the map. The jetting mode is only identified in the map with high We .

By the comparison between several specific images, the boundary of the dripping mode and jetting mode zones can be assumed. As Figure 4-2 shows, the length of the DP stream between the needle tip and the pinch-off drop is increased with Ca increasing. The experimental result of $Q_d = 4$ mL/min and $V_c = 376.9$ mm/s is very close to the jetting mode. From this comparison, a hypothesis is that the jetting mode related with Ca . For higher Ca , the jetting mode should occur. More experiments will be considered for supporting the assumption as future works.

Mode	
Hollow marks	Dripping
Solid marks	Jetting
V_c [mm/s]	
○	140.3
☆	189.0
□	210.4
▽	280.6
◇	283.6
△	378.1
D_{needle} (inner diameter) [mm]	
Small marks	0.14
Big marks	0.32
Q_d [mL/min]	
Red	0.1
Green	0.5
Blue	1
Black	2
Yellow	4
Cyan	6
Magenta	8

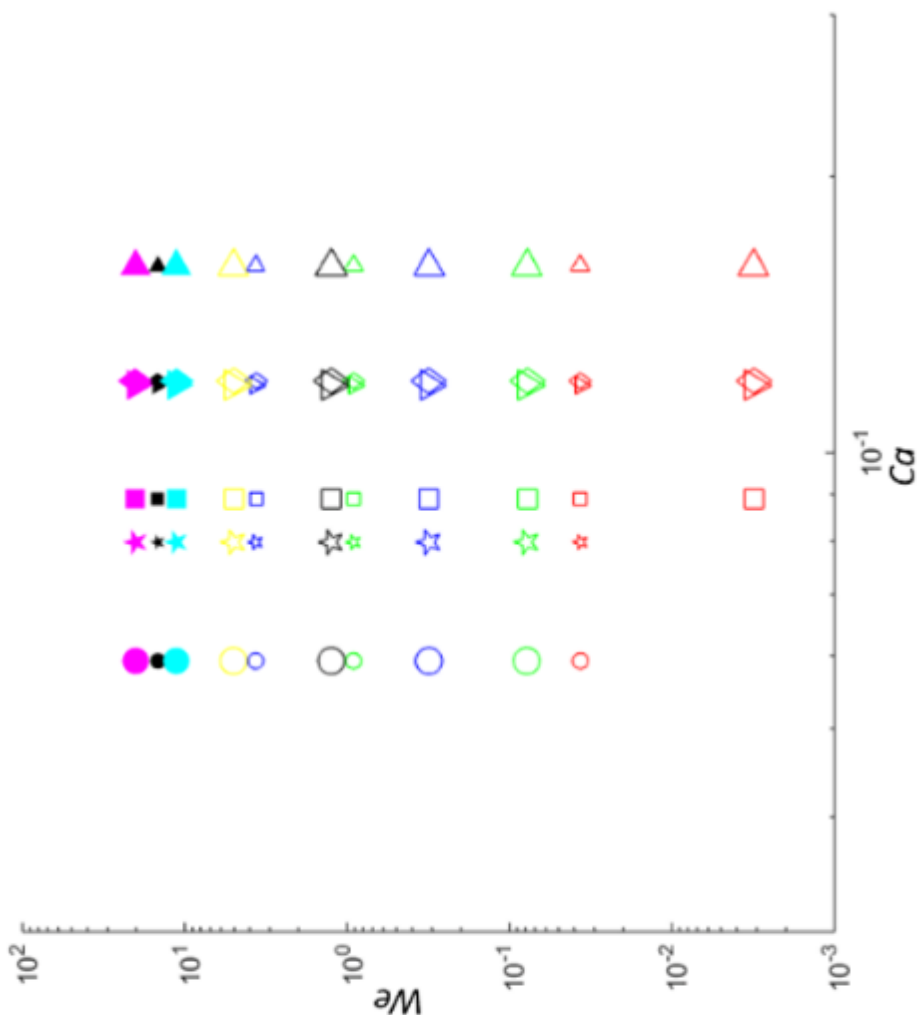


Figure 4-1-1. The nondimensional number-based map ($Ca-We$).

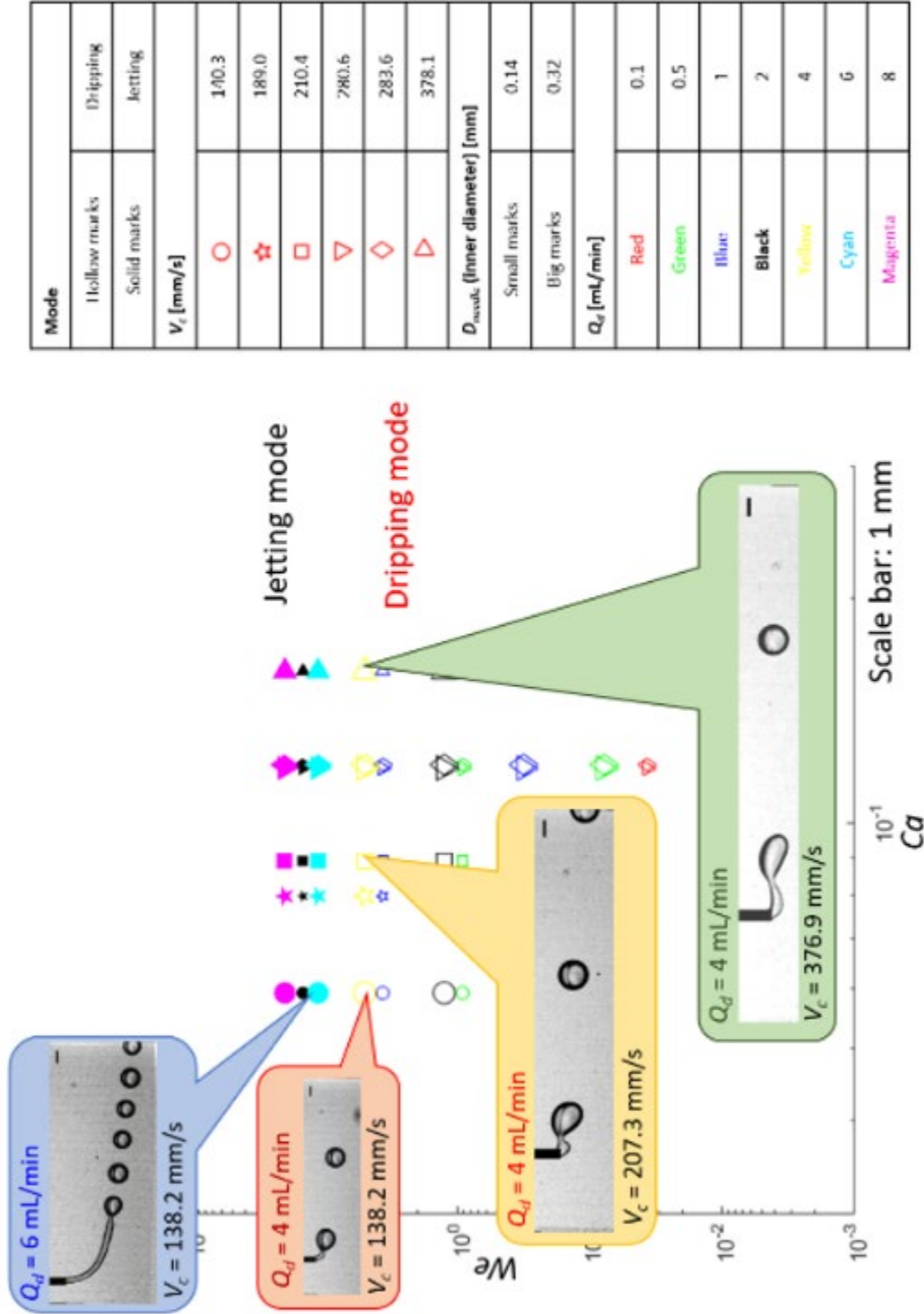


Figure 4-2. The prediction of the pinch-off zones in Ca-We map.

Considering the effect of Oh [2, 21, 38], Oh_{CP} and the value of Ca/Oh_{CP} are calculated as Table D-2. Figure 4-3 is the $Ca/Oh-We$ -based map from the calculation results. The map can be compared with the frame in Figure 4-4 with same range [38]. The jetting mode occur in high We for both Figure 4-3 and 4-4, but the values of We at DJT are different. DJT can be found at $We = 10$ and $We = 1$, respectively. A possible reason of this difference is the experimental setup. For the data in Figure 4-3, because rotational rigid body motion of CP was used for the shear force, CP was considered as uniform flow. However, for the data in Figure 4-4, CP was applied through a cylindrical channel with wall shear stress. Following studies of the DJT difference will be considered as future works.

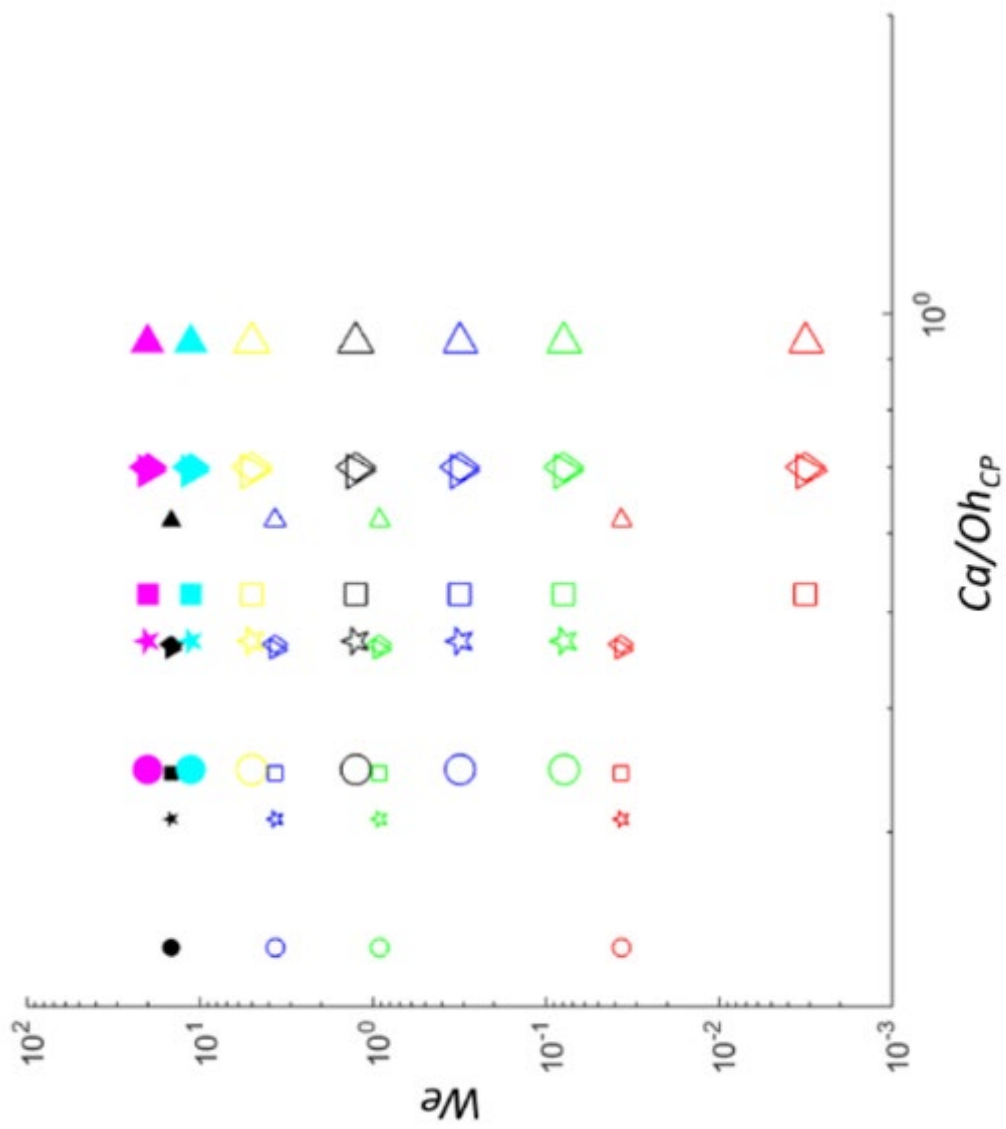


Figure 4-3. The nondimensional number-based map (Ca/Oh_{CP} - We).

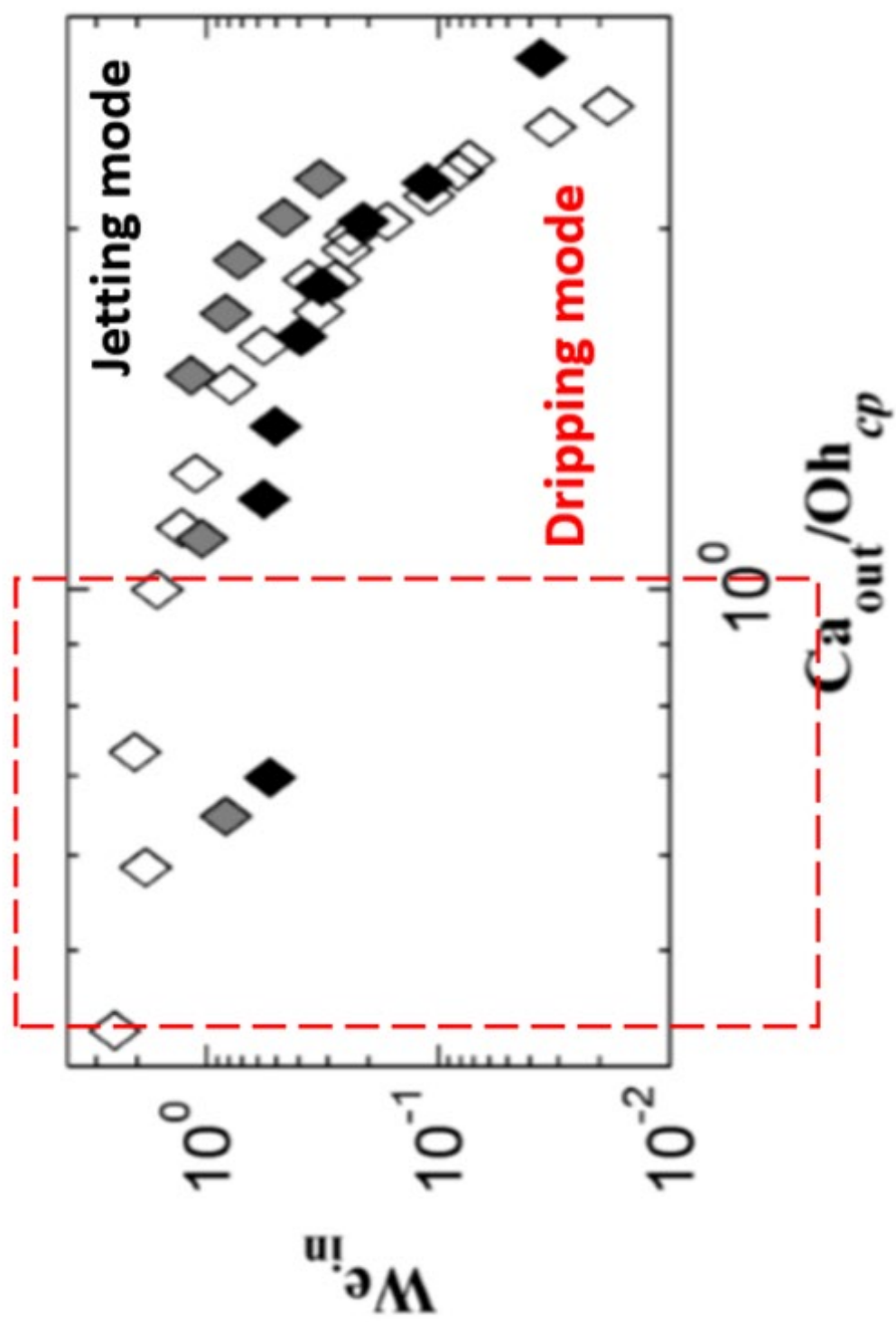


Figure 4-4. The comparison of nondimensional number-based map ($Ca/Oh-We$) [38].

4.4 Drop Size Predictions in Torque Balance Equation

As the introduction shows, torque balance equation (TBE) is another way to predict D_{drop} from the experimental conditions [13, 27-29, 31, 43-45]. TBE is a model based on the drops generated in the dripping mode. Drops are pinched off when the torques of forces acting on the drop reached balanced state. Drops in the jetting mode cannot be predicted by TBE because of different process of pinch-off.

Figure 4-5 is the schematic figure of the TBE in this study. The drop is pinched off from the joint. Drag force (F_{DR}), surface tension force (F_{γ}), Young-Laplace force (F_{YL}), buoyancy force (F_{BG}), and gravity (F_G) are calculated as Eq. (4-1) to Eq. (4-5), respectively [12, 25, 29, 43, 46-51]. C_D and A_{drop} in Eq. (4-1) are the drag coefficient and the cross-section area of the drop, V_{drop} in Eq. (4-4) and Eq. (4-5) are the volume of the drop, respectively. The drop is assumed as spherical shape without deformation.

$$F_{DR} = C_D A_{drop} \frac{\rho_c V_c^2}{2}, \quad (4-1)$$

$$F_{\gamma} = \pi D_{needle} \gamma, \quad (4-2)$$

$$F_{YL} = \frac{\gamma}{D_{drop}} \pi D_{needle}^2, \quad (4-3)$$

$$F_{BG} = \rho_c g V_{drop}, \quad (4-4)$$

$$F_G = \rho_d g V_{drop}, \quad (4-5)$$

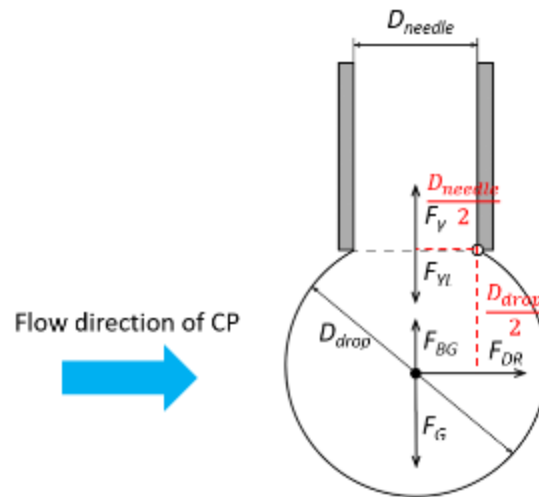


Figure 4-5. The schematic figure of TBE in this study.

Dynamic lift force is not considered because the shear rate is 0 for uniform flow of CP. The inertia force of DP is ignored based on the assumption that the pressure difference because of DP at the needle tip is smaller than the Laplace pressure at the curved surface of DP [43].

For C_D , different values are used in literatures. Either a Reynolds number related equation or a correction factor for specific experimental setup are determined [23, 38, 42, 60]. In this study, the drag coefficient of sphere, $C_D = 0.47$, was used.

As the figure shows, the arms of forces are simplified as $\frac{D_{needle}}{2}$ and $\frac{D_{drop}}{2}$, respectively. The TBE for this study is summarized as Eq. (4-6) [43].

$$F_{DR} \frac{D_{drop}}{2} = (F_V - F_{YL} - F_G + F_{BG}) \frac{D_{needle}}{2}, \quad (4-6)$$

Substituting the known values based on different experimental conditions, D_{drop} can be solved from Eq. (4-6). Imaginary roots and root do not meaningful, such as $D_{drop} = D_{needle}$, are ignored. The chosen solutions of D_{drop} in different experimental conditions are summarized as Table E-1.

The solved D_{drop} were introduced in the dimensionless map to compare with the experimental data as Figure 4-6 and 4-7. Solved D_{drop} were plotted with corresponding experimental conditions of D_{needle} , V_d , and V_c . The solid lines connected the experimental data of D_{drop} with dripping modes, and the dashed lines indicates D_{drop} solved from TBE.

From the experimental data, D_{drop} increased with V_d . But this relationship is not shown in D_{drop} solved from TBE. The reason is the lack of V_d in the equation of TBE. Only V_c is included in the term of drag force, so the result changing because of V_d cannot be presented.

Also, the solved D_{drop} showed difference between the experimental data, which may cause by the model of TBE. TBE is based on one assumption that no deformation occurs during the pinch-off process. The drop is considered as a rigid sphere with forces acting on it. It is not true because fluid cannot maintain the shape under stresses. When forces are acting on the drop, the drop will deform and flow away. Since the model ignored the nature of fluid, D_{drop} solved from TBE can have limitation for drop size predictions.

Mode	
Hollow marks	Dripping
Solid marks	Jetting
V_c [mm/s]	
○	140.3
☆	189.0
□	210.4
▽	280.6
◇	283.6
△	378.1
Q_d [mL/min]	
Red	0.1
Green	0.5
Blue	1
Black	2

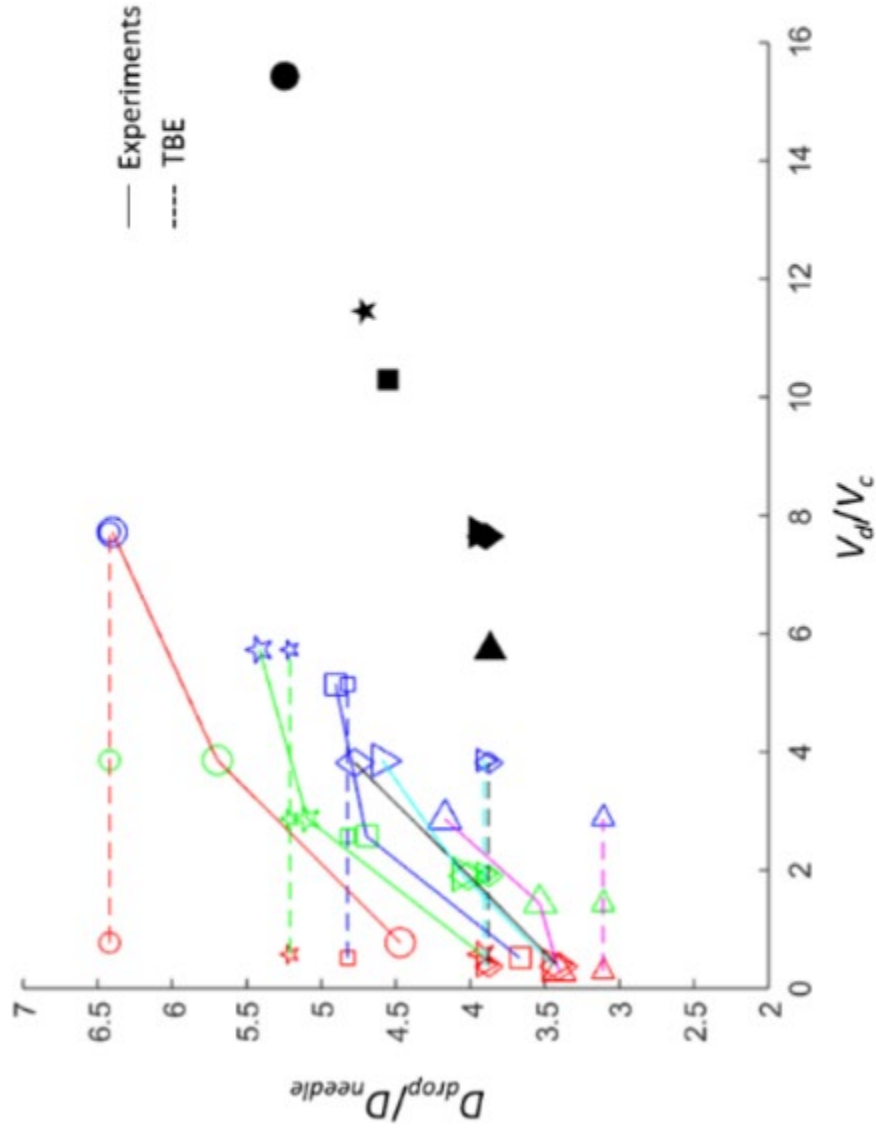


Figure 4-6. The comparison of D_{drop} between TBE and experimental data. ($D_{needle} = 0.14$ mm)

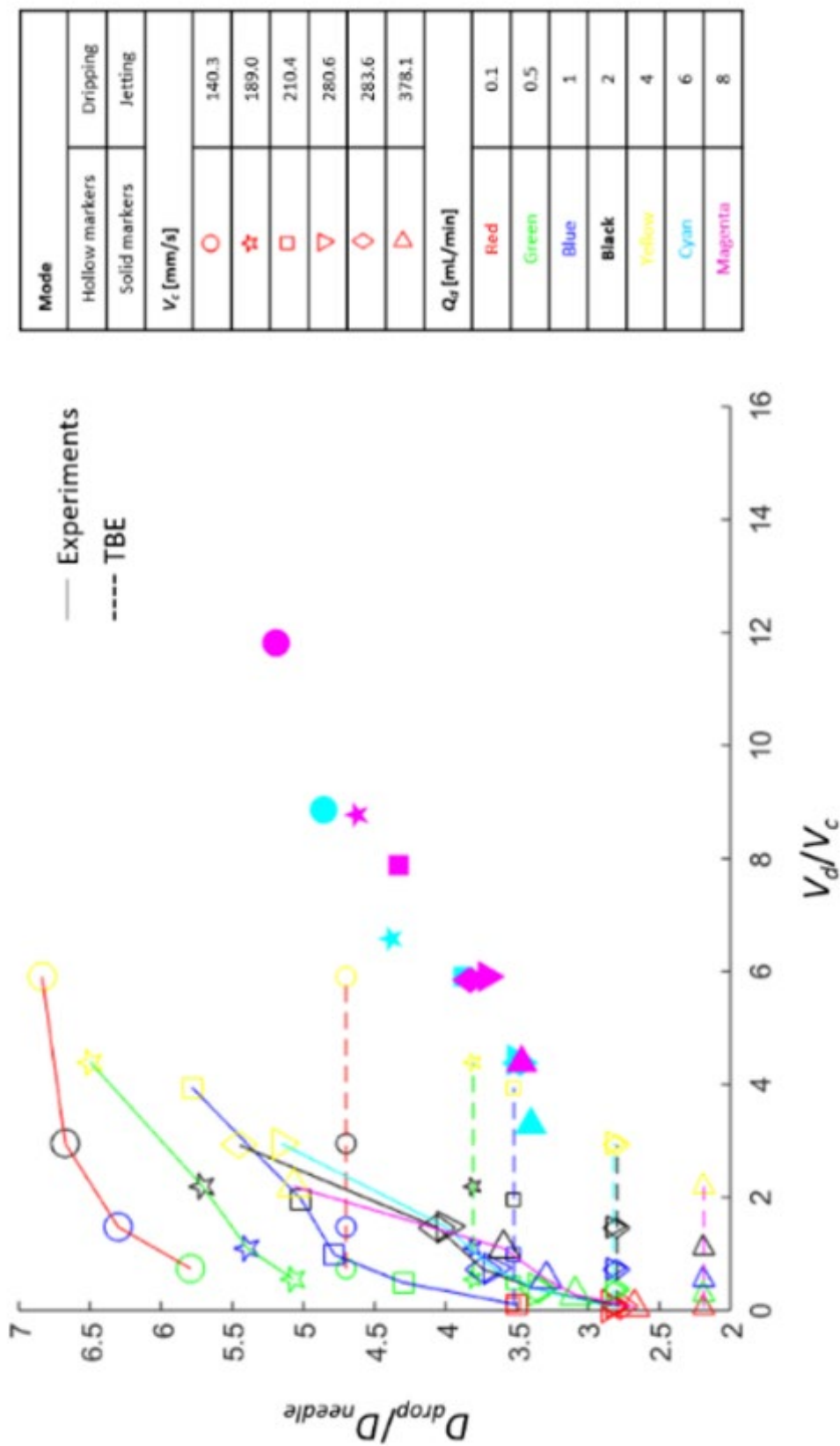


Figure 4-7. The comparison of D_{drop} between TBE and experimental data. ($D_{needle} = 0.32 \text{ mm}$)

Chapter 5 Conclusion

In this study, a cross-flow based drop generator was developed based on the CP in rotational rigid body motion. The DP was injected into the CP through a needle perpendicularly to the motion of the CP. Shear force because of the rotational motion of CP generated drops of DP in the setup. Also, the range of D_{drop} can be changed by applying different experimental conditions.

Two different pinch-off modes, the dripping mode and the jetting mode, were observed in the system with different experimental conditions. The jetting mode can occur with high V_d . In the dripping mode, drops were detached from the needle tip one by one. In the jetting mode, drops were generated from the rapture of elongated DP stream in the CP. Increased surface area of DP and the tendency of DP to minimize the surface area caused the wavy shape of the DP stream. Eventually the unstable DP stream raptured as multiple drops. Comparing with the drops in the dripping modes, the drops in the jetting modes were smaller and not monodispersed.

Software ADM was used to measure D_{drop} from captured images. The monodispersity of generated drops were compared with other methods. Drops were monodispersed in the dripping mode than in the jetting mode, and drops generated in both of these modes were acceptable.

Nondimensional analysis phase diagram map, V_d/V_c and D_{drop}/D_{needle} , was used to predict D_{drop} with known experimental conditions. It was possible to check the D_{drop} from the map as reference values.

Ca , We , and Oh were studied to predict the pinch-off mode. For higher Ca and We ,

jetting mode will occur. The specific DJT for different pairs of CP and DP are different. Oh can be used to understand the effect of different fluids. It was possible to predict the pinch-off mode from the experimental conditions.

The DJT in $Ca-We-Oh$ -based map was different with references. The reason can be the difference between experimental setups. Following studies will be considered as future works.

Also, D_{drop} solved from TBE were compared with experimental data. TBE showed limitations of D_{drop} prediction. The difference between TBE solved results and experimental data can be caused by the assumption of TBE. As a conclusion, TBE does not work well for the setup in this study.

In summary, it was possible to make different sized drops by controlling the experimental conditions of the setup. In future, applications of making hydrogel beads with controllable sized are considered [65, 66]. Solutions of hydrogel will be used as the DP. By changing the experimental conditions, various sizes of hydrogel solution drops can be generated. After gelation process, hydrogel beads can be collected from the setup.

Appendix A. The Measurement Results of Drop Sizes

Table A-1. The drop diameters with various experimental conditions.

V_c [mm/s]	V_d [mm/s]	D_{drop} [μm] (mean \pm std)
140.28	108.73	625.70 ± 14.25
	543.67	797.43 ± 5.03
	1087.34	896.16 ± 51.10
	2174.68	734.26 ± 34.33
189.04	108.73	549.29 ± 4.27
	543.67	712.96 ± 3.55
	1087.34	758.01 ± 3.39
	2174.68	659.41 ± 58.69
210.42	108.73	513.71 ± 7.67
	543.67	657.59 ± 8.88
	1087.34	686.41 ± 3.58
	2174.68	636.90 ± 39.19
283.56	108.73	477.83 ± 2.97
	543.67	561.57 ± 2.57
	1087.34	668.54 ± 24.89
	2174.68	546.48 ± 21.58

(Continued)

V_c [mm/s]	V_d [mm/s]	D_{drop} [μm] (mean \pm std)
280.57	108.73	482.51 ± 3.10
	543.67	567.64 ± 3.72
	1087.34	642.92 ± 25.65
	2174.68	552.62 ± 20.16
378.08	108.73	476.73 ± 3.24
	543.67	494.73 ± 1.77
	1087.34	583.79 ± 5.70
	2174.68	541.30 ± 5.89
140.28	105.26	1853.60 ± 68.88
	210.51	2016.70 ± 7.49
	421.02	2135.40 ± 11.55
	842.04	2187.40 ± 149.60
	1263.06	1554.40 ± 75.65
	1684.08	1661.40 ± 196.32
189.04	105.26	1622.00 ± 4.87
	210.51	1725.70 ± 4.97
	421.02	1826.60 ± 5.65
	842.04	2078.50 ± 12.46
	1263.06	1402.20 ± 83.56
	1684.08	1479.50 ± 220.48

(Continued)

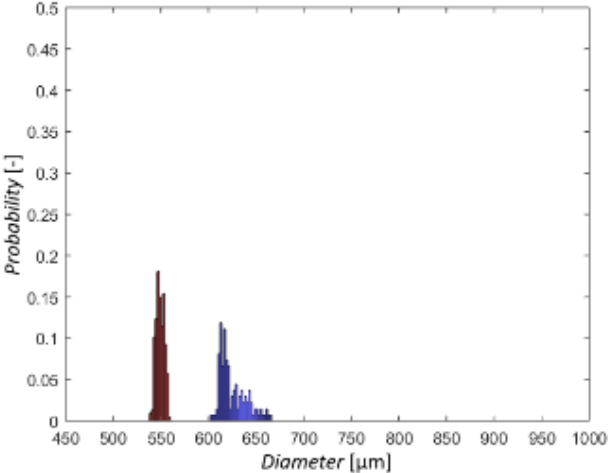
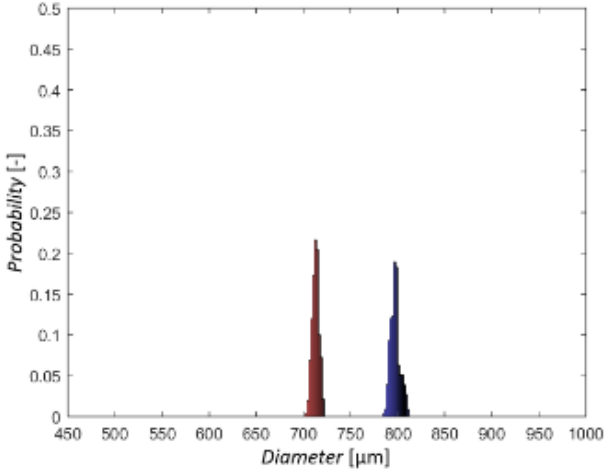
V_c [mm/s]	V_d [mm/s]	D_{drop} [μm] (mean \pm std)
210.42	21.05	1119.50 \pm 4.31
	105.26	1376.40 \pm 6.42
	210.51	1530.60 \pm 18.64
	421.02	1605.40 \pm 4.55
	842.04	1849.70 \pm 8.82
	1263.06	1241.60 \pm 34.83
	1684.08	1384.70 \pm 172.51
283.56	21.05	888.20 \pm 14.30
	105.26	1071.30 \pm 10.83
	210.51	1196.60 \pm 10.00
	421.02	1298.00 \pm 32.52
	842.04	1743.20 \pm 35.42
	1263.06	1112.70 \pm 122.39
	1684.08	1223.80 \pm 144.82

(Continued)

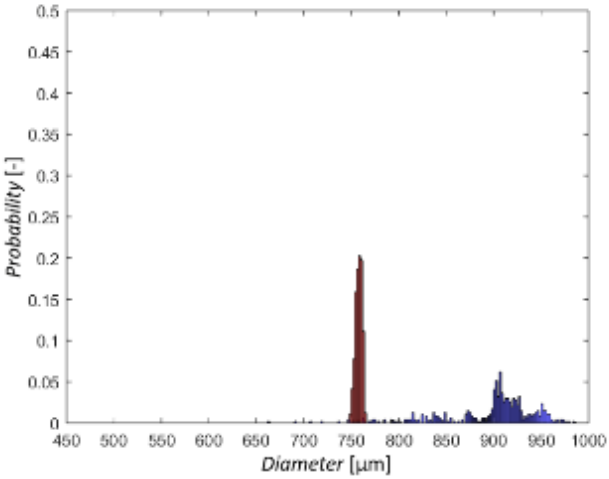
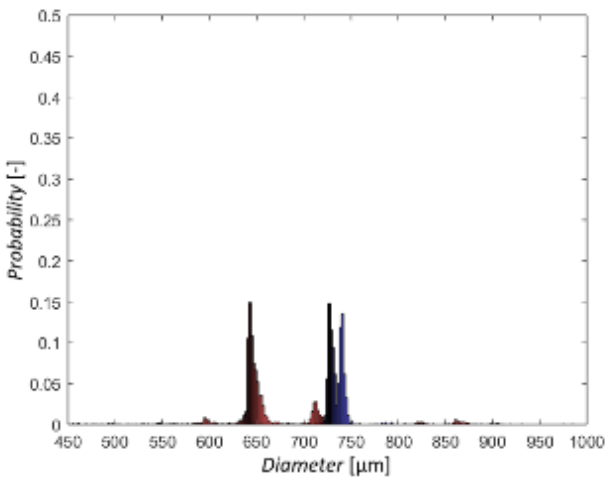
V_c [mm/s]	V_d [mm/s]	D_{drop} [μm] (mean \pm std)
280.57	21.05	909.81 \pm 1.88
	105.26	1074.20 \pm 77.26
	210.51	1173.20 \pm 34.17
	421.02	1279.40 \pm 2.50
	842.04	1649.90 \pm 14.70
	1263.06	1121.40 \pm 111.68
	1684.08	1187.20 \pm 167.99
378.08	21.05	855.51 \pm 1.58
	105.26	988.49 \pm 44.63
	210.51	1053.80 \pm 65.24
	421.02	1149.20 \pm 37.33
	842.04	1621.40 \pm 164.63
	1263.06	1088.20 \pm 120.74
	1684.08	1109.4 \pm 139.57

Appendix B. The Size Distributions of Generated Drops

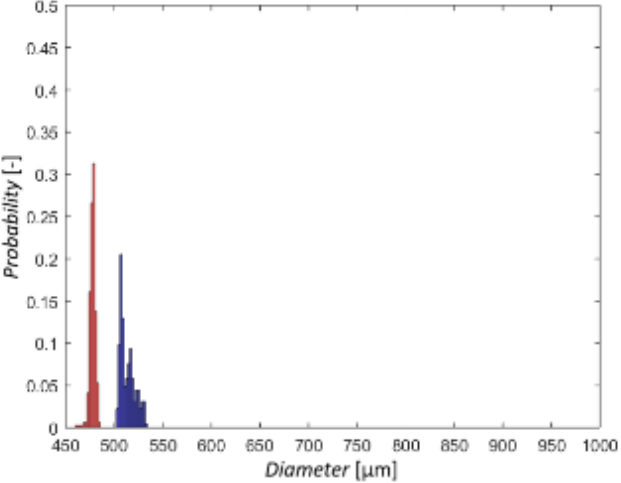
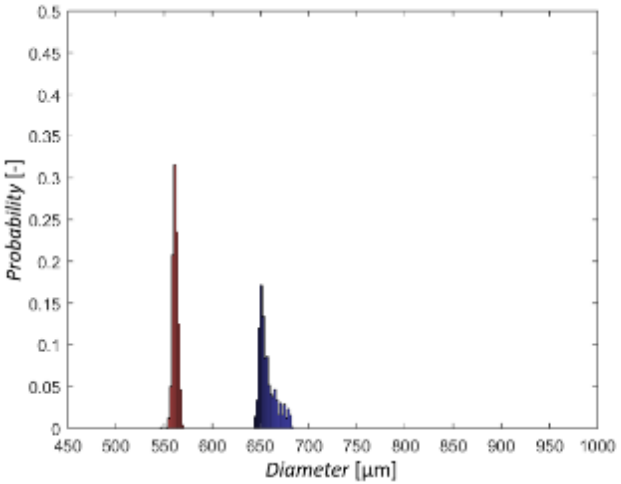
Table B-1. The histograms of experiments with $D_{needle} = 0.14$ mm.

V_c [mm/s] V_d [mm/s]	<div style="text-align: center; color: blue;">140.28</div> <div style="text-align: center; color: red;">189.04</div>	Mode
	108.73	
543.67		Dripping

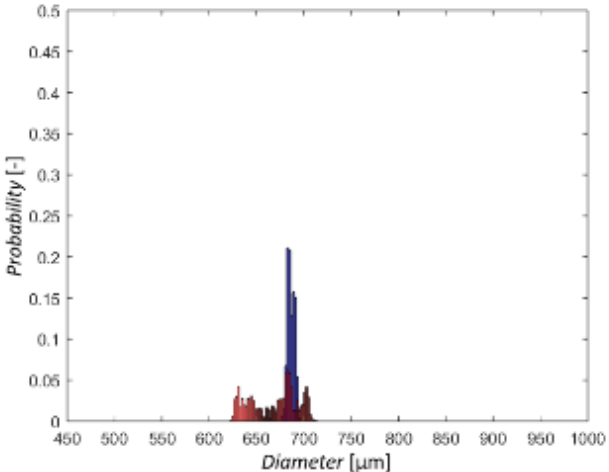
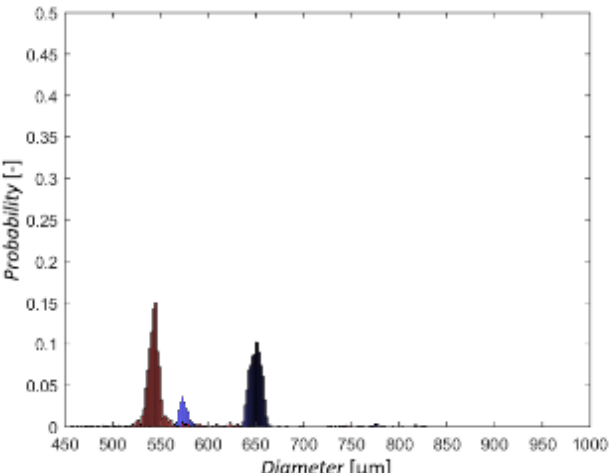
(Continued)

V_c [mm/s] V_d [mm/s]	<p style="text-align: center;">140.28</p> <p style="text-align: center;">189.04</p>	<p style="text-align: center;">Mode</p>
<p style="text-align: center;">1087.34</p>		<p style="text-align: center;">Dripping</p>
<p style="text-align: center;">2174.68</p>		<p style="text-align: center;">Jetting</p>

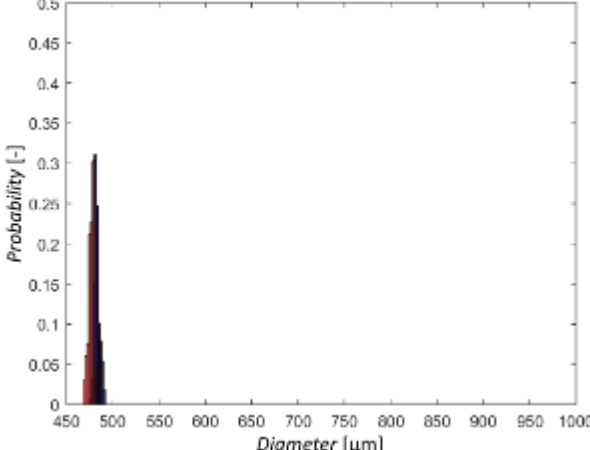
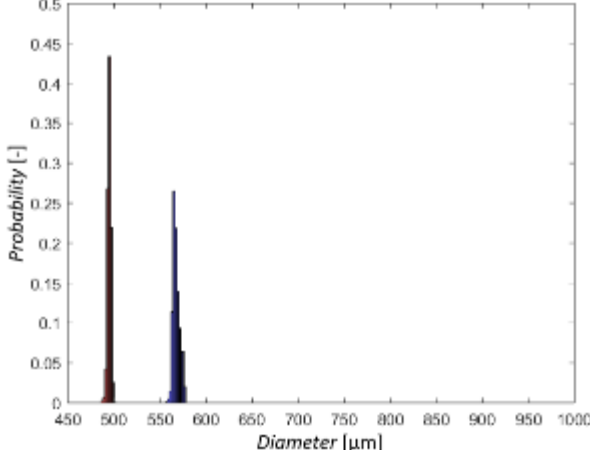
(Continued)

V_c [mm/s] V_d [mm/s]	<p style="text-align: center;">210.42</p> <p style="text-align: center;">283.56</p>	<p style="text-align: center;">Mode</p>
<p style="text-align: center;">108.73</p>		<p style="text-align: center;">Dripping</p>
<p style="text-align: center;">543.67</p>		<p style="text-align: center;">Dripping</p>

(Continued)

V_c [mm/s] V_d [mm/s]	<p style="text-align: center;">210.42</p> <p style="text-align: center;">283.56</p>	<p style="text-align: center;">Mode</p>
<p style="text-align: center;">1087.34</p>		<p style="text-align: center;">Dripping</p>
<p style="text-align: center;">2174.68</p>		<p style="text-align: center;">Jetting</p>

(Continued)

V_c [mm/s] V_d [mm/s]	<p>280.57</p> <p>378.08</p>	Mode
108.73		Dripping
543.67		Dripping

(Continued)

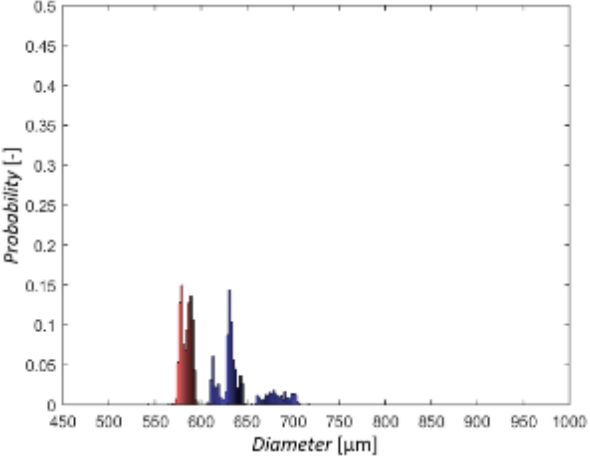
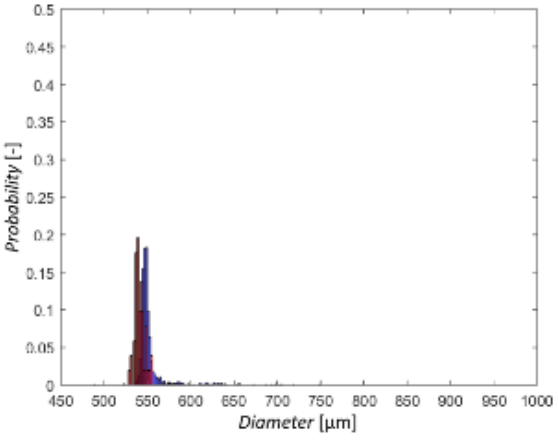
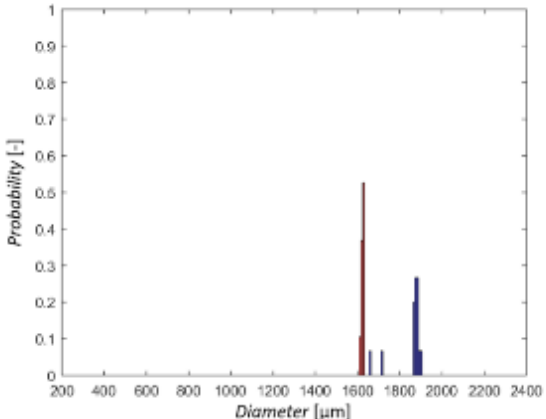
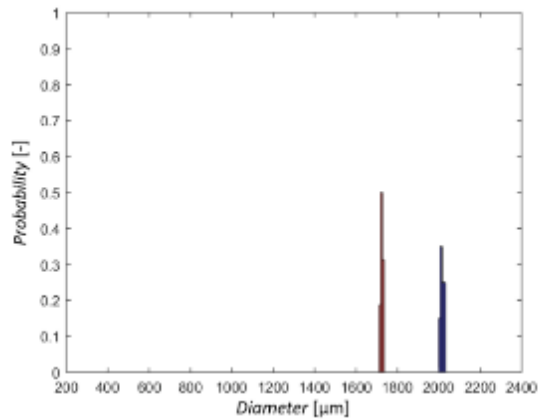
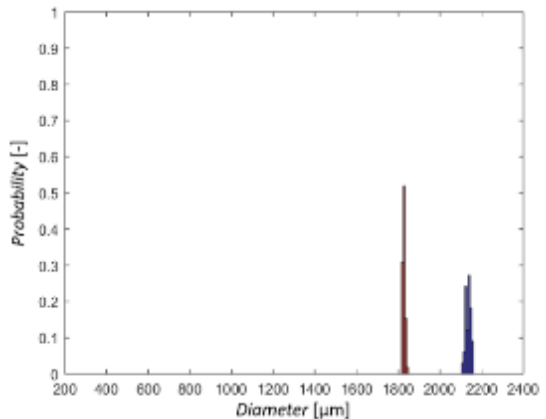
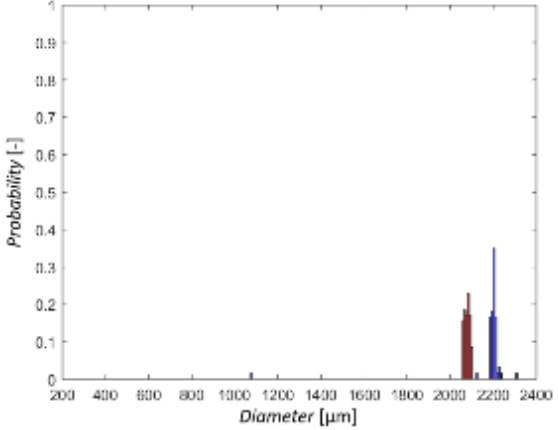
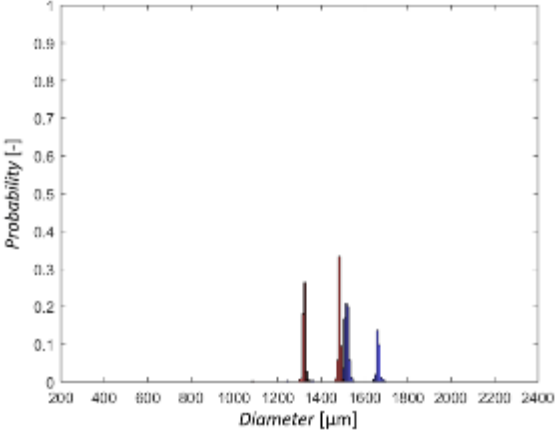
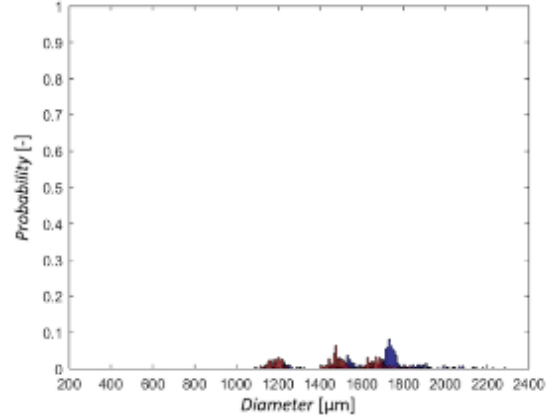
V_c [mm/s] V_d [mm/s]	<p style="text-align: center;">280.57</p> <p style="text-align: center;">378.08</p>	<p style="text-align: center;">Mode</p>
<p style="text-align: center;">1087.34</p>		<p style="text-align: center;">Dripping</p>
<p style="text-align: center;">2174.68</p>		<p style="text-align: center;">Jetting</p>

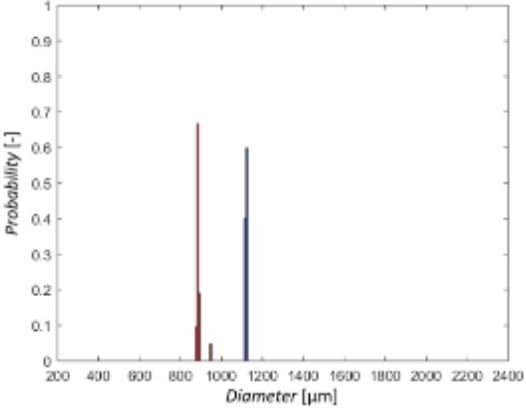
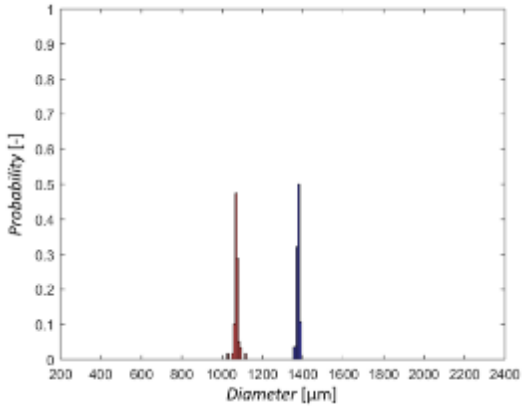
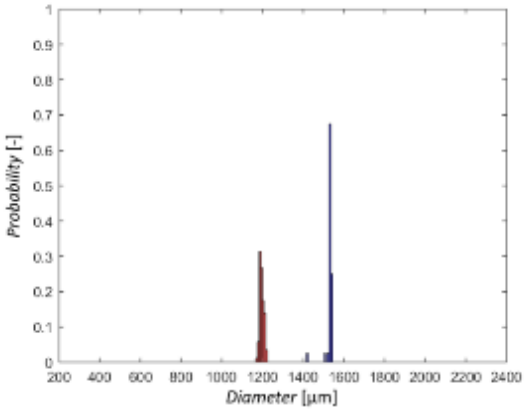
Table B-2. The histograms of experiments with $D_{needle} = 0.32$ mm.

V_c [mm/s] V_d [mm/s]	140.28 189.04	Mode
	105.26	
210.51		Dripping
421.02		Dripping

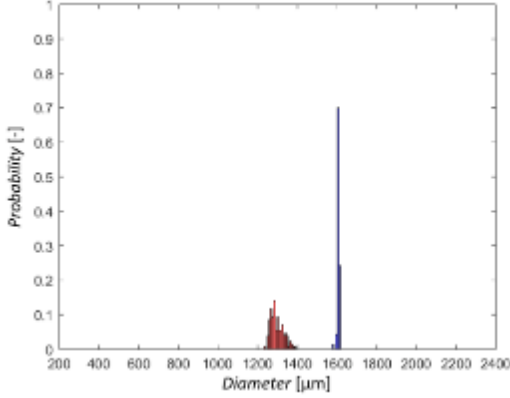
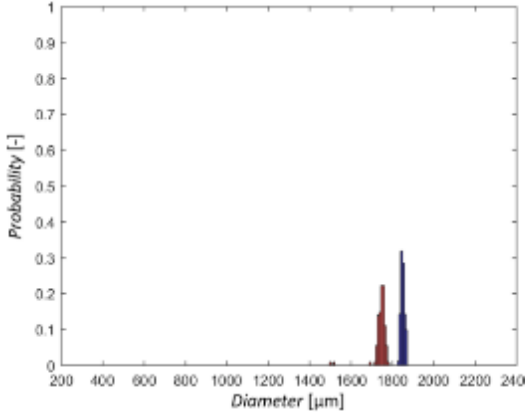
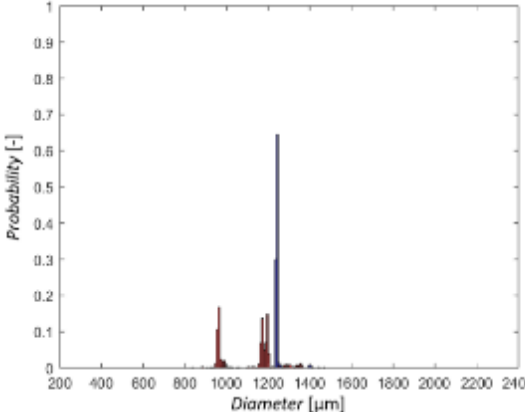
(Continued)

V_c [mm/s] V_d [mm/s]	<p style="text-align: center;">140.28</p> <p style="text-align: center;">189.04</p>	<p style="text-align: center;">Mode</p>
<p style="text-align: center;">842.04</p>		<p style="text-align: center;">Dripping</p>
<p style="text-align: center;">1263.06</p>		<p style="text-align: center;">Jetting</p>
<p style="text-align: center;">1684.08</p>		<p style="text-align: center;">Jetting</p>

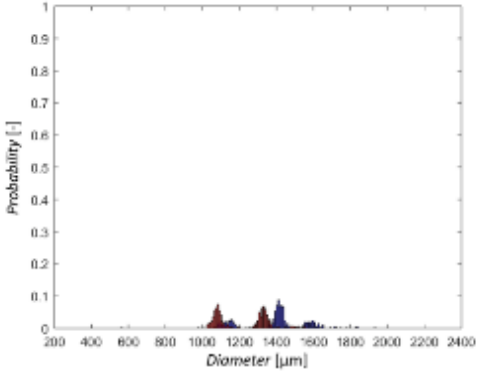
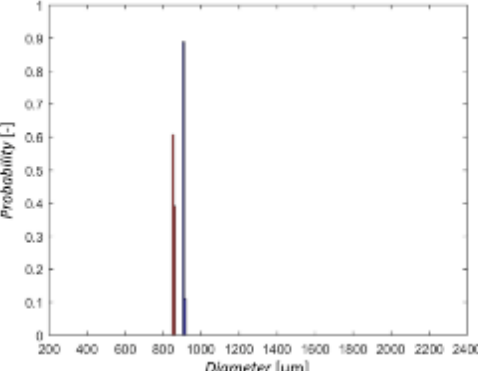
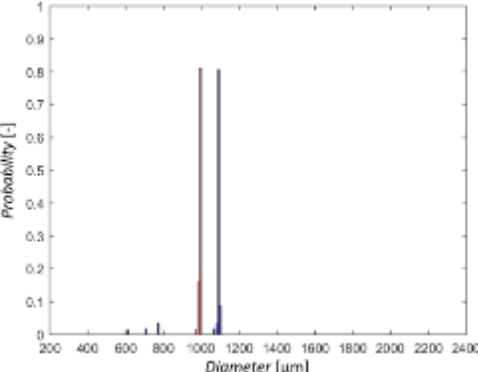
(Continued)

V_c [mm/s] V_d [mm/s]	<p style="text-align: center;">210.42</p> <p style="text-align: center;">283.56</p>	<p style="text-align: center;">Mode</p>
<p style="text-align: center;">21.05</p>		<p style="text-align: center;">Dripping</p>
<p style="text-align: center;">105.26</p>		<p style="text-align: center;">Dripping</p>
<p style="text-align: center;">210.51</p>		<p style="text-align: center;">Dripping</p>

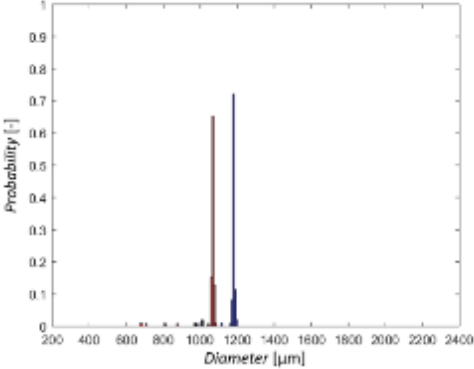
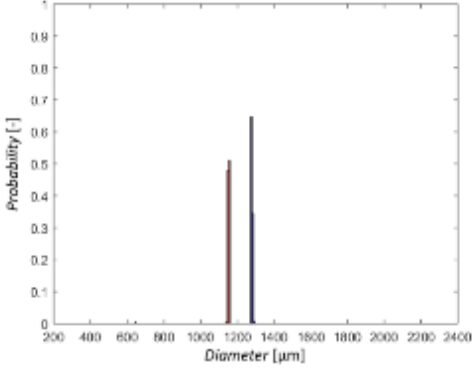
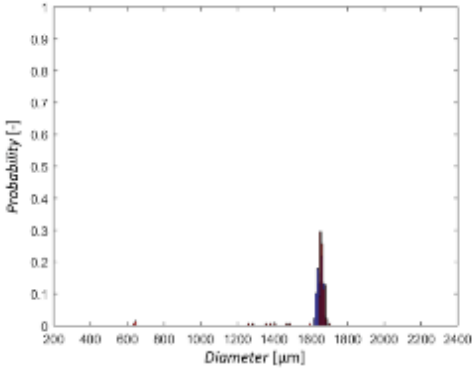
(Continued)

V_c [mm/s] V_d [mm/s]	<p style="text-align: center;">210.42</p> <p style="text-align: center;">283.56</p>	<p style="text-align: center;">Mode</p>
<p style="text-align: center;">421.02</p>		<p style="text-align: center;">Dripping</p>
<p style="text-align: center;">842.04</p>		<p style="text-align: center;">Dripping</p>
<p style="text-align: center;">1263.06</p>		<p style="text-align: center;">Jetting</p>

(Continued)

V_c [mm/s] V_d [mm/s]	<p style="text-align: center;">210.42</p> <p style="text-align: center;">283.56</p>	<p style="text-align: center;">Mode</p>
<p style="text-align: center;">1684.08</p>		<p style="text-align: center;">Jetting</p>
V_c [mm/s] V_d [mm/s]	<p style="text-align: center;">280.57</p> <p style="text-align: center;">378.08</p>	<p style="text-align: center;">Mode</p>
<p style="text-align: center;">21.05</p>		<p style="text-align: center;">Dripping</p>
<p style="text-align: center;">105.26</p>		<p style="text-align: center;">Dripping</p>

(Continued)

V_c [mm/s] V_d [mm/s]	<p style="text-align: center;">280.57</p> <p style="text-align: center;">378.08</p>	<p style="text-align: center;">Mode</p>
<p style="text-align: center;">210.51</p>		<p style="text-align: center;">Dripping</p>
<p style="text-align: center;">421.02</p>		<p style="text-align: center;">Dripping</p>
<p style="text-align: center;">842.04</p>		<p style="text-align: center;">Dripping</p>

(Continued)

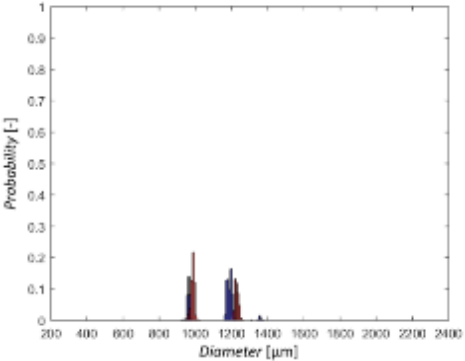
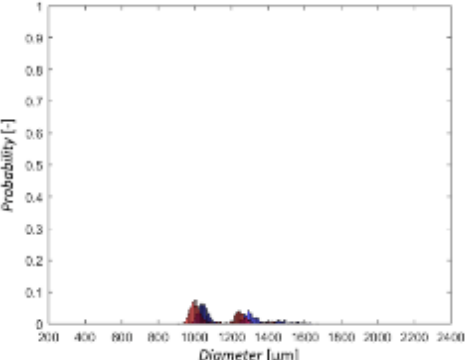
V_c [mm/s] V_d [mm/s]	<p style="text-align: center;">280.57</p> <p style="text-align: center;">378.08</p>	<p style="text-align: center;">Mode</p>
<p style="text-align: center;">1263.06</p>		<p style="text-align: center;">Jetting</p>
<p style="text-align: center;">1684.08</p>		<p style="text-align: center;">Jetting</p>

Table B-3. The calculation results of CV.

D_{needle} [mm]	V_c [mm/s]	V_d [mm/s]	CV [%]
0.14	140.28	108.73	2.3
		543.67	0.63
		1087.34	5.7
		2174.68	4.7
	189.04	108.73	0.78
		543.67	0.50
		1087.34	0.45
		2174.68	8.90
	210.42	108.73	1.49
		543.67	1.35
		1087.34	0.52
		2174.68	6.15

(Continued)

D_{needle} [mm]	V_c [mm/s]	V_d [mm/s]	CV [%]
0.14	283.56	108.73	0.62
		543.67	0.46
		1087.34	3.72
		2174.68	3.95
	280.57	108.73	0.64
		543.67	0.65
		1087.34	3.99
		2174.68	3.65
	378.08	108.73	0.68
		543.67	0.36
		1087.34	0.98
		2174.68	1.09

(Continued)

D_{needle} [mm]	V_c [mm/s]	V_d [mm/s]	CV [%]
0.32	140.28	105.26	3.72
		210.51	0.37
		421.02	0.54
		842.04	6.84
		1263.06	4.87
		1684.08	11.82
	189.04	105.26	0.30
		210.51	0.29
		421.02	0.31
		842.04	0.60
		1263.06	5.96
		1684.08	14.90
	210.42	21.05	0.38
		105.26	0.47
		210.51	1.22
		421.02	0.28
		842.04	0.48
		1263.06	2.81
		1684.08	12.46

(Continued)

D_{needle} [mm]	V_c [mm/s]	V_d [mm/s]	CV [%]
0.32	283.56	21.05	1.61
		105.26	1.01
		210.51	0.84
		421.02	2.51
		842.04	2.03
		1263.06	11.00
		1684.08	11.83
		280.57	21.05
	105.26		7.19
	210.51		2.91
	421.02		0.20
	842.04		0.89
	1263.06		9.96
	1684.08		14.15
	378.08	21.05	0.19
		105.26	4.51
		210.51	6.19
		421.02	3.25
		842.04	10.15
		1263.06	11.10
		1684.08	12.58

Appendix C. The Calculation of Dimensionless Parameters

Table C-1. The parameters of the nondimensional analysis.

D_{needle} [mm]	V_c [mm/s]	V_d [mm/s]	V_d/V_c	D_{drop}/D_{needle}
0.14	140.28	108.73	0.77	4.47
		543.67	3.86	5.70
		1087.34	7.72	6.40
		2174.68	15.43	5.24
	189.04	108.73	0.57	3.92
		543.67	2.86	5.09
		1087.34	5.73	5.41
		2174.68	11.46	4.71
	210.42	108.73	0.51	3.67
		543.67	2.57	4.70
		1087.34	5.15	4.90
		2174.68	10.29	4.55

(Continued)

D_{needle} [mm]	V_c [mm/s]	V_d [mm/s]	V_d/V_c	D_{drop}/D_{needle}
0.14	283.56	108.73	0.38	3.41
		543.67	1.91	4.01
		1087.34	3.82	4.78
		2174.68	7.64	3.90
	280.57	108.73	0.39	3.45
		543.67	1.93	4.05
		1087.34	3.86	4.59
		2174.68	7.72	3.95
	378.08	108.73	0.29	3.41
		543.67	1.43	3.53
		1087.34	2.86	4.17
		2174.68	5.73	3.87

(Continued)

D_{needle} [mm]	V_c [mm/s]	V_d [mm/s]	V_d/V_c	D_{drop}/D_{needle}
0.32	140.28	105.26	0.74	5.79
		210.51	1.48	6.30
		421.02	2.95	6.67
		842.04	5.91	6.84
		1263.06	8.86	4.86
		1684.08	11.82	5.19
	189.04	105.26	0.55	5.07
		210.51	1.10	5.39
		421.02	2.19	5.71
		842.04	4.39	6.50
		1263.06	6.58	4.38
		1684.08	8.77	4.62
	210.42	21.05	0.10	3.50
		105.26	0.49	4.30
		210.51	0.98	4.78
		421.02	1.97	5.02
		842.04	3.94	5.78
		1263.06	5.91	3.88
		1684.08	7.88	4.33

(Continued)

D_{needle} [mm]	V_c [mm/s]	V_d [mm/s]	V_d/V_c	D_{drop}/D_{needle}
0.32	283.56	21.05	0.07	2.78
		105.26	0.37	3.35
		210.51	0.73	3.74
		421.02	1.46	4.06
		842.04	2.92	5.45
		1263.06	4.38	3.48
		1684.08	5.85	3.82
	280.57	21.05	0.07	2.84
		105.26	0.37	3.36
		210.51	0.74	3.67
		421.02	1.48	4.00
		842.04	2.95	5.16
		1263.06	4.43	3.50
		1684.08	5.91	3.71
	378.08	21.05	0.05	2.67
		105.26	0.27	3.09
		210.51	0.55	3.29
		421.02	1.10	3.59
		842.04	2.19	5.07
		1263.06	3.29	3.40
		1684.08	4.38	3.47

Appendix D. The Calculation of Nondimensional Numbers

Table D-1. The calculations of the nondimensional numbers (Ca and We).

D_{needle} [mm]	V_c [mm/s]	V_d [mm/s]	Ca	We
0.14	140.28	108.73	59.2	0.036706657
		543.67		0.917733957
		1087.34		3.670935828
		2174.68		14.68374331
	189.04	108.73	79.8	0.036706657
		543.67		0.917733957
		1087.34		3.670935828
		2174.68		14.68374331
	210.42	108.73	88.8	0.036706657
		543.67		0.917733957
		1087.34		3.670935828
		2174.68		14.68374331

(Continued)

D_{needle} [mm]	V_c [mm/s]	V_d [mm/s]	Ca	We
0.14	283.56	108.73	119.7	0.036706657
		543.67		0.917733957
		1087.34		3.670935828
		2174.68		14.68374331
	280.57	108.73	118.5	0.036706657
		543.67		0.917733957
		1087.34		3.670935828
		2174.68		14.68374331
	378.08	108.73	159.6	0.036706657
		543.67		0.917733957
		1087.34		3.670935828
		2174.68		14.68374331

(Continued)

D_{needle} [mm]	V_c [mm/s]	V_d [mm/s]	Ca	We
0.32	140.28	105.26	59.2	0.07863117
		210.51		0.3144948
		421.02		1.257979198
		842.04		5.031916792
		1263.06		11.32181278
		1684.08		20.12766717
	189.04	105.26	79.8	0.07863117
		210.51		0.3144948
		421.02		1.257979198
		842.04		5.031916792
		1263.06		11.32181278
		1684.08		20.12766717
	210.42	21.05	88.8	0.003144649
		105.26		0.07863117
		210.51		0.3144948
		421.02		1.257979198
		842.04		5.031916792
		1263.06		11.32181278
1684.08		20.12766717		

(Continued)

D_{needle} [mm]	V_c [mm/s]	V_d [mm/s]	Ca	We
0.32	283.56	21.05	119.7	0.003144649
		105.26		0.07863117
		210.51		0.3144948
		421.02		1.257979198
		842.04		5.031916792
		1263.06		11.32181278
		1684.08		20.12766717
		280.57		21.05
	105.26		0.07863117	
	210.51		0.3144948	
	421.02		1.257979198	
	842.04		5.031916792	
	1263.06		11.32181278	
	1684.08		20.12766717	
	378.08		21.05	159.6
		105.26	0.07863117	
		210.51	0.3144948	
		421.02	1.257979198	
		842.04	5.031916792	
		1263.06	11.32181278	
		1684.08	20.12766717	

Table D-2. The calculations of the nondimensional numbers (Oh_{CP} and Ca/Oh_{CP}).

D_{needle} [mm]	V_c [mm/s]	V_d [mm/s]	Oh_{CP}	Ca/Oh_{CP}
0.14	140.28	108.73	0.258127	0.229458
		543.67		
		1087.34		
		2174.68		
	189.04	108.73		0.309215
		543.67		
		1087.34		
		2174.68		
	210.42	108.73		0.344187
		543.67		
		1087.34		
		2174.68		

(Continued)

D_{needle} [mm]	V_c [mm/s]	V_d [mm/s]	Oh_{CP}	Ca/Oh_{CP}
0.14	283.56	108.73	0.258127	0.463823
		543.67		
		1087.34		
		2174.68		
	280.57	108.73		0.458932
		543.67		
		1087.34		
		2174.68		
	378.08	108.73		0.618430
		543.67		
		1087.34		
		2174.68		

(Continued)

D_{needle} [mm]	V_c [mm/s]	V_d [mm/s]	Oh_{CP}	Ca/Oh_{CP}
0.32	140.28	105.26	0.170735	0.346908
		210.51		
		421.02		
		842.04		
		1263.06		
		1684.08		
	189.04	105.26		0.467489
		210.51		
		421.02		
		842.04		
		1263.06		
		1684.08		
	210.42	21.05		0.520361
		105.26		
		210.51		
		421.02		
		842.04		
		1263.06		
		1684.08		

(Continued)

D_{needle} [mm]	V_c [mm/s]	V_d [mm/s]	Oh_{CP}	Ca/Oh_{CP}
0.32	283.56	21.05	0.170735	0.701234
		105.26		
		210.51		
		421.02		
		842.04		
		1263.06		
		1684.08		
	280.57	21.05		0.693840
		105.26		
		210.51		
		421.02		
		842.04		
		1263.06		
		1684.08		
378.08	21.05	0.934979		
	105.26			
	210.51			
	421.02			
	842.04			
	1263.06			
	1684.08			

Appendix E. The Calculation of Torque Balance Equation

Table E-1. The calculations of D_{drop} using TBE.

D_{needle} [mm]	V_c [mm/s]	V_d [mm/s]	D_{drop} [μm]
0.14	140.28	108.73	898.7
		543.67	
		1087.34	
		2174.68	
	189.04	108.73	729.3
		543.67	
		1087.34	
		2174.68	
	210.42	108.73	675.5
		543.67	
		1087.34	
		2174.68	

(Continued)

D_{needle} [mm]	V_c [mm/s]	V_d [mm/s]	D_{drop} [μm]
0.14	283.56	108.73	542.7
		543.67	
		1087.34	
		2174.68	
	280.57	108.73	547.0
		543.67	
		1087.34	
		2174.68	
	378.08	108.73	435.3
		543.67	
		1087.34	
		2174.68	

(Continued)

D_{needle} [mm]	V_c [mm/s]	V_d [mm/s]	D_{drop} [μm]
0.32	140.28	105.26	1503.9
		210.51	
		421.02	
		842.04	
		1263.06	
		1684.08	
	189.04	105.26	1218.6
		210.51	
		421.02	
		842.04	
		1263.06	
		1684.08	
	210.42	210.42	21.05
105.26			
210.51			
421.02			
842.04			
1263.06			
1684.08			

(Continued)

D_{needle} [mm]	V_c [mm/s]	V_d [mm/s]	D_{drop} [μm]
0.32	283.56	21.05	894.5
		105.26	
		210.51	
		421.02	
		842.04	
		1263.06	
		1684.08	
	280.57	21.05	902.2
		105.26	
		210.51	
		421.02	
		842.04	
		1263.06	
		1684.08	
	378.08	21.05	699.9
		105.26	
		210.51	
		421.02	
		842.04	
		1263.06	
		1684.08	

References

1. R. Seemann, M.B., T. Pfohl and S. Herminghaus, *Droplet Based Microfluidics*. Rep. Prog. Phys., 2011. **75**(1): p. 016601.
2. Wang, P.Z.a.L., *Passive and Active Droplet Generation with Microfluidics: A Review*. Lab Chip, 2017. **17**(1): p. 34-75.
3. Schramm, L.L., *Emulsions, Foams, and Suspensions: Fundamentals and Applications* 2006: John Wiley & Sons.
4. Anna, G.F.C.a.S.L., *Microfluidic Methods for Generating Continuous Droplet Streams*. J. Phys. D, 2007. **40**(19): p. R319.
5. S. Y. Teh, R.L., L. H. Hung and A. P. Lee, *Droplet Microfluidics*. Lab Chip, 2008. **8**(2): p. 198-220.
6. M. Abkarian, E.L., and G. Massiera, *Continuous Droplet Interface Crossing Encapsulation (cDICE) for High Throughput Monodisperse Vesicle Design*. Soft Matter, 2011. **7**(10): p. 4610-4614.
7. A. Rakszewska, J.T., V. Chokkalingam and W. T. S. Huck, *One Drop at A Time: Toward Droplet Microfluidics as A Versatile Tool for Single-cell Analysis*. NPG Asia Mater., 2014. **6**: p. e133.
8. J. F. Edd, D.D.C., K. J. Humphry, S. Köster, D. Irimia, D. A. Weitz and M. Toner, *Controlled Encapsulation of Single-cells into Monodisperse Picolitre Drops*. Lab Chip, 2008. **8**(8): p. 1262-1264.
9. Trägårdh, S.M.J.a.G., *Membrane Emulsification—A Literature Review*. J. Membr. Sci. , 2000. **169**(1): p. 107-117.
10. V. Trivedi, A.D., G. K. Kurup, E. Ereifej, P. J. Vandevord and A. S. Basu, *A Modular Approach for the Generation, Storage, Mixing, and Detection of Droplet Libraries for High Throughput Screening*. Lab Chip, 2010. **10**(18): p. 2433-2442.
11. I. Ziemecka, V.v.S., G. J. M. Koper, M. Rosso, A. M. Brizard, J. H. van Esch and M. T. Kreutzer, *Monodisperse Hydrogel Microspheres by Forced Droplet Formation in Aqueous Two-phase Systems*. Lab Chip, 2011. **11**(4): p. 620-624.
12. R. Ito, Y.H., K. Inoue and Y. Kitagawa, *Formation of Liquid Drop through a Nozzle in Uniform Stream*. Kagaku Kougaku Ronbunshu 1979. **5**(3): p. 288-292.
13. Williams, S.J.P.a.R.A., *Controlled Production of Emulsions Using a Crossflow Membrane: Part I: Droplet Formation from a Single Pore*. Chem. Eng. Res. Des. , 1998. **76**(8): p. 894-901.
14. Peng, S.J. and R.A. Williams, *Controlled Production of Emulsions Using a Crossflow Membrane: Part I: Droplet Formation from a Single Pore*. Chemical Engineering Research and Design, 1998. **76**(8): p. 894-901.
15. R. A. Williams, S.J.P., D. A. Wheeler, N. C. Morley, D. Taylor, M. Whalley and D. W. Houldsworth, *Controlled Production of Emulsions Using a Crossflow Membrane: Part II: Industrial Scale Manufacture*. Chem. Eng. Res. Des. , 1998. **76**(8): p. 902-910.
16. A. J. Gijbetsen-Abrahamse, A.v.d.P.a.R.M.B., *Status of Cross-flow Membrane Emulsification and Outlook for Industrial Application*. J. Membr. Sci. , 2004. **230**(1-2): p. 149-159.

17. I. Kobayashi, M.N., K. Chun, Y. Kikuchi and H. Fujita, *Silicon Array of Elongated through-holes for Monodisperse Emulsion Droplets*. *AIChE J.*, 2002. **48**(8): p. 1639-1644.
18. T. Nisisako, T.T.a.T.H., *Droplet Formation in a Microchannel Network*. *Lab Chip*, 2002. **2**(1): p. 24-26.
19. Pit, A., M. Duits, and F. Mugele, *Droplet manipulations in two phase flow microfluidics*. *Micromachines*, 2015. **6**(11): p. 1768-1793.
20. Anna, S.L., *Droplets and Bubbles in Microfluidic Devices*. *Annu. Rev. Fluid Mech.*, 2016. **48**: p. 285-309.
21. Crocker, R.F.M.a.J.C., *Universal Dripping and Jetting in a Transverse Shear Flow*. *Phys. Rev. Lett.*, 2009. **102**(19): p. 194501.
22. A. J. Abrahamse, R.v.L., R. G. M. van der Sman, A. van der Padt and R. M. Boom, *Analysis of Droplet Formation and Interactions During Cross-flow Membrane Emulsification*. *J. Membr. Sci.* , 2002. **204**(1-2): p. 125-137.
23. J. Zawala, K.S.a.P.W., *Theoretical and Experimental Studies of Drop Size in Membrane Emulsification—Single Pore Studies of Hydrodynamic Detachment of Droplets*. *Colloids Surf. A*, 2015. **470**: p. 297-305.
24. D. X. Hao, F.L.G., G. H. Hu, Y. J. Zhao, G. P. Lian, G. H. Ma and Z. G. Su, *Controlling Factors on Droplets Uniformity in Membrane Emulsification: Experiment and Modeling Analysis*. *Ind. Eng. Chem. Res.*, 2008. **47**(17): p. 6418-6425.
25. N. C. Christov, K.D.D., D. K. Danova and P. A. Kralchevsky, *The Drop Size in Membrane Emulsification Determined From the Balance of Capillary and Hydrodynamic Forces*. *Langmuir*, 2008. **24**(4): p. 1397-1410.
26. G. De Luca, A.D.R., F. P. Di Maio and E. Drioli, *Modelling Droplet Formation in Cross-flow Membrane Emulsification*. *Desalination*, 2006. **199**(1-3): p. 177-179.
27. M. J. Geerken, R.G.H.L.a.M.W., *Interfacial Aspects of Water Drop Formation at Micro-engineered Orifices*. *J. Colloid Interface Sci.* , 2007. **312**(2): p. 460-469.
28. A. Timgren, G.T.a.C.T., *A Model for Drop Size Prediction during Cross-flow Emulsification*. *Chem. Eng. Res. Des.*, 2010. **88**(2): p. 229-238.
29. Trägårdh, M.R.a.G., *Membrane Emulsification Modelling: How can We Get from Characterisation to Design?* *Desalination*, 2002. **145**(1-3): p. 165-172.
30. K. Feigl, F.X.T., S. Holzapfel and E. J. Windhab, *Effect of Flow Type, Channel Height, and Viscosity on Drop Production from Micro-pores*. *Chem. Eng. Sci.*, 2014. **116**: p. 372-382.
31. Z. Wang, S.C.W., V. Schroeder and H. Schubert, *Influence of Fluid Flow on Forces Acting on Droplet and Emulsification Results in Membrane Emulsification Process*. *Chin. J. Chem. Eng.* , 1999. **50**(4): p. 505-513.
32. A. M. Pit, M.H.G.D.a.F.M., *Droplet Manipulations in Two Phase Flow Microfluidics*. *Micromachines*, 2015. **6**(11): p. 1768-1793.
33. T. Thorsen, R.W.R., F. H. Arnold and S. R. Quake, *Depletion Interactions and Fractionated Crystallization for Polydisperse Emulsion Purification* *Phys. Rev. Lett*, 2001. **86**: p. 4163-4166.
34. P. Garstecki, I.G., W. DiLuzio, G. M. Whitesides, E. Kumacheva and H. A. Stone, *Formation of Monodisperse Bubbles in a Microfluidic Flow-focusing Device*. *Appl. Phys. Lett.*, 2004. **85**(13): p. 2649-2651.
35. B. Zheng, J.D.T.a.R.F.I., *Formation of Droplets of Alternating Composition in Microfluidic*

- Channels and Applications to Indexing of Concentrations in Droplet-based Assays.* Anal. Chem. , 2004. **76**(17): p. 4977-4982.
36. P. Garstecki, M.J.F., H. A. Stone and G. M. Whitesides, *Formation of Droplets and Bubbles in a Microfluidic T-junction—Scaling and Mechanism of Break-up.* Lab Chip, 2006. **6**(3): p. 437-446.
 37. Zhang, H.H.L.a.Y.H., *Droplet Formation in a T-shaped Microfluidic Junction.* J. Appl. Phys., 2009. **106**(3): p. 034906.
 38. A. Bertrandias, H.D., J. Casalinho and M. L. Giorgi, *Dripping to Jetting Transition for Cross-flowing Liquids.* Phys. Fluids, 2017. **29**(4): p. 044102.
 39. É. Lepercq-Bost, M.L.G., A. Isambert and C. Arnaud, *Use of the Capillary Number for the Prediction of Droplet Size in Membrane Emulsification.* J. Membr. Sci. , 2008. **314**(1-2): p. 76-89.
 40. S. Zhang, C.G.-C., S. Veessler and N. Candoni, *Prediction of Sizes and Frequencies of Nanoliter-sized Droplets in Cylindrical T-junction Microfluidics.* Chem. Eng. Sci., 2015. **138**: p. 128-139.
 41. A. S. Utada, L.Y.C., A. Fernandez-Nieves, D. R. Link, C. Holtze and D. A. Weitz, *Dripping, Jetting, Drops, and Wetting: The Magic of Microfluidics.* MRS Bull., 2007. **32**(9): p. 702-708.
 42. Pathak, M., *Numerical Simulation of Membrane Emulsification: Effect of Flow Properties in the Transition from Dripping to Jetting.* J. Membr. Sci. , 2011. **382**(1-2): p. 166-176.
 43. G. De Luca, F.P.D.M., A. Di Renzo and E. Drioli, *Droplet Detachment in Cross-flow Membrane Emulsification: Comparison among Torque-and Force-based Models.* Chem. Eng. Process., 2008. **47**(7): p. 1150-1158.
 44. Wang, Z.W.a.S.C., *Effect of Continuous Phase Viscosity on Membrane Emulsification.* Chin. J. Chem. Eng. , 2000. **8**(2): p. 108-112.
 45. G. De Luca, A.S., L. Giorno and E. Drioli, *Quantitative Analysis of Coupling Effects in Cross-flow Membrane Emulsification.* J. Membr. Sci. , 2004. **229**(1-2): p. 199-209.
 46. A. Timgren, G.T.a.C.T., *Application of the PIV Technique to Measurements around and inside a Forming Drop in a Liquid-liquid System.* Exp. Fluids, 2008. **44**(4): p. 565-575.
 47. Pathak, M., *Numerical Simulation of Droplet Dynamics in Membrane Emulsification Systems*, in *Numerical Simulation-From Theory to Industry2012*, InTech.
 48. Ulbrecht, Y.K.a.J.J., *Formation of Drops and Bubbles in Flowing Liquids.* Ind. Eng. Chem. Process Des. Dev., 1981. **20**(4): p. 636-640.
 49. V. Schröder, O.B.a.H.S., *Effect of Dynamic Interfacial Tension on the Emulsification Process Using Microporous, Ceramic Membranes.* J. Colloid Interface Sci. , 1998. **202**(2): p. 334-340.
 50. M. Rayner, G.T., C. Trägårdh and P. Dejmek, *Using the Surface Evolver to Model Droplet Formation Processes in Membrane Emulsification.* J. Colloid Interface Sci. , 2004. **279**(1): p. 175-185.
 51. J. H. Xu, G.S.L., G. G. Chen and J. D. Wang, *Experimental and Theoretical Approaches on Droplet Formation from a Micrometer Screen Hole.* J. Membr. Sci. , 2005. **266**(1-2): p. 121-131.
 52. O. E. Yildirim, Q.X.a.O.A.B., *Analysis of the Drop Weight Method.* Phys. Fluids, 2005. **17**(6): p. 062107.

53. Tolman, R.C., *The Effect of Droplet Size on Surface Tension*. J. Chem. Phys., 1949. **17**(3): p. 333-337.
54. Demarquette, E.Y.A.a.N.R., *Use of the Pendant Drop Method to Measure Interfacial Tension Between Molten Polymers*. Mater. Res., 1999. **2**(1): p. 23-32.
55. B. B. Lee, P.R.a.E.S.C., *New Drop Weight Analysis for Surface Tension Determination of Liquids*. Colloids Surf. A, 2009. **332**(2-3): p. 112-120.
56. M. D. Abramoff, P.J.M.a.S.J.R., *Image Processing with ImageJ*. Biophotonics international. Vol. 11. 2004. 36-42.
57. C. A. Schneider, W.S.R.a.K.W.E., *NIH Image to ImageJ: 25 years of Image Analysis*. Nat. Methods, 2012. **9**(7): p. 671.
58. Z. Z. Chong, S.B.T., A. M. Gañán-Calvo, Z. J. Chong, N. H. Loh, N. T. Nguyen and S. H. Tan, *Automated Droplet Measurement (ADM): An Enhanced Video Processing Software for Rapid Droplet Measurements*. Microfluid. Nanofluid., 2016. **20**(4): p. 66.
59. Z. Z. Chong, S.H.T., A. M. Gañán-Calvo, S. B. Tor, N. H. Loh and N. T. Nguyen, *Active Droplet Generation in Microfluidics*. Lab Chip, 2016. **16**(1): p. 35-58.
60. R. F. Meyer, W.B.R., M. T. McClendon and J. C. Crocker, *Producing Monodisperse Drug-loaded Polymer Microspheres via Cross-flow Membrane Emulsification: The Effects of Polymers and Surfactants*. Langmuir, 2010. **26**(18): p. 14479-14487.
61. J. H. Xu, S.W.L., J. Tan, Y. J. Wang and G. S. Luo, *Preparation of Highly Monodisperse Droplet in a T-junction Microfluidic Device*. AIChE Journal, 2006. **52**(9): p. 3005-3010.
62. F. Malloggi, N.P., R. Attia, F. Monti, P. Mary, H. Willaime, P. Tabeling, B. Cabane and P. Poncet, *Monodisperse Colloids Synthesized with Nanofluidic Technology*. Langmuir, 2009. **26**(4): p. 2369-2373.
63. G. T. Vladislavljević, I.K.a.M.N., *Production of Uniform Droplets Using Membrane, Microchannel and Microfluidic Emulsification Devices*. Microfluid. Nanofluid., 2012. **13**(1): p. 151-178.
64. M. M. Dragosavac, G.T.V., R. G. Holdich and M. T. Stillwell, *Production of Porous Silica Microparticles by Membrane Emulsification*. Langmuir, 2011. **28**(1): p. 134-143.
65. L. Y. Chu, A.S.U., R. K. Shah, J. W. Kim and D. A. Weitz, *Controllable Monodisperse Multiple Emulsions*. Angew. Chem., 2007. **119**(47): p. 9128-9132.
66. D. Saeki, S.S., T. Kanamori, S. Sato and S. Ichikawa, *Formation of Monodisperse Calcium Alginate Microbeads by Rupture of Water-in-oil-in-water Droplets with an Ultra-thin Oil Phase Layer*. Lab Chip, 2010. **10**(17): p. 2292-2295.